RESEARCH ARTICLE

Key Points:
- A > 4-km-thick serpentinized mantle layer beneath thin crust within continent-ocean transition indicates limited melt supply during rifting
- While all three continental crustal layers extended depth dependently, they pinched out together against the transitional zone seaward
- Synrift extension was amagmatic on both conjugate margins but with asymmetry resulting from postrift volcanism on the Moroccan margin

Correspondence to:
K. W. H. Lau,
kwhlau@dal.ca

Continent-Ocean Transition Across the Northeastern Nova Scotian Margin From a Dense Wide-Angle Seismic Profile

K. W. H. Lau[1], Mladen R. Nedimović[1], and Keith E. Louden[1]

[1]Department of Earth Sciences, Dalhousie University, Halifax, Nova Scotia, Canada

Abstract To improve constraints on rifting processes resulting in the formation of the southeastern Canadian margin, we interpret the most detailed regional 2-D velocity model from offshore Nova Scotia constructed using wide-angle OETR-2009 data. This 405-km-long profile was collected with 78 ocean bottom seismometers. The presented data analysis and interpretation are supported by a reflection image from the coincident long streamer GXT-2000 profile. We identify a continental zone where the full-thickness (~30 km), three-layered continental crust beneath the inner shelf thins sharply seaward by a listric fault that forms a 12-km-deep Huron Subbasin beneath a high-velocity carbonate bank (~5.8 km/s), creating a shadow zone above tilted crustal blocks. Depth-dependent and variable initial thinning is evidenced in all three modeled crustal layers, which, nevertheless, pinch out together at their seaward ends. More gradual and regional thinning and a local amagmatic thickening are modeled seaward beneath the slope until 70 km from the shelf break, beyond which a deepwater amagmatic continent-ocean transition shows velocity characteristics not typical of either continental or oceanic crust. The 100-km-wide continent-ocean transition is characterized by a low-velocity (5.3–5.4 km/s), low gradient, <2-km thick upper crust, above a high-velocity (6.3–7.5 km/s), high gradient, <5-km-thick lower crust, which can be interpreted as moderately serpentinized mantle. Underneath this layer is a <5-km-thick low-velocity (7.1–8.0 km/s) partially serpentinized mantle layer. A ~5-km-thick oceanic crust is modeled seaward. Our results suggest that amagmatic processes dominated the continental breakup in this area.

1. Introduction

The Nova Scotia continental margin is marked by a first-order change in rifting architecture, as it transitions from the magma-rich U.S. East Coast margins (Holbrook & Kelemen, 1993) in the south to the magma-poor Grand Bank/Newfoundland margin (Lau et al., 2006) in the north. Magma-rich margins are noted for continent-ocean transitions (COTs) with seaward-dipping reflections (SDRs) indicative of magma extrusion onto the basement and thick igneous underplate beneath or within the thinned lower continental crust (e.g., Talwani & Abreu, 2000). Magma-poor margins show COTs characterized by thin oceanic crust and sometimes exposed and serpentinized mantle indicative of limited to no melt generation (e.g., Louden & Chian, 1999; Ros et al., 2017). While some of these characteristic features have been interpreted on individual profiles across the Nova Scotia margin, the nature of where and how the transition between magma-rich and magma-poor regions occurs is still uncertain.

A classic volcanic margin for the southwestern Nova Scotia offshore was initially suggested by 2-D crustal-scale multichannel seismic (MCS) reflection profiles, based on the coincidence of SDRs and the high-amplitude (~300 nT) East Coast Magnetic Anomaly (ECMA; Keen & Potter, 1995a). In the northeast Nova Scotia offshore, where the ECMA is absent (Figure 1), another MCS profile (Keen & Potter, 1995b) shows no SDRs and a subsequent coincident wide-angle survey (SMART-1) using ocean bottom seismometers (OBSs) indicates a crustal transition to a margin type more typical of a magma-poor margin (Funck et al., 2004). Within the central Nova Scotia offshore section, although the ECMA may still be present, it is much weaker (180–200 nT; Keen et al., 1991) and SDRs have not been observed (Keen et al., 1991; Keen & Cordsen, 1981). A further wide-angle survey (SMART-2) in this region (Wu et al., 2006) shows a complex structure within the COT, which is atypical of either magma-rich or magma-poor stereotypes. More recently, the NovaSPAN industry MCS profiles, referred to as GXT profiles in this paper (Figure 1), suggest that the magmatic-to-amagmatic transition occurs in the southwestern part of the margin (Louden et al., 2013).

Subsequent to these previous studies, a dense wide-angle profile OETR-2009 (Figure 1) was acquired across the northeastern Nova Scotia margin for the Offshore Energy Research Association of Nova Scotia by GeoPro
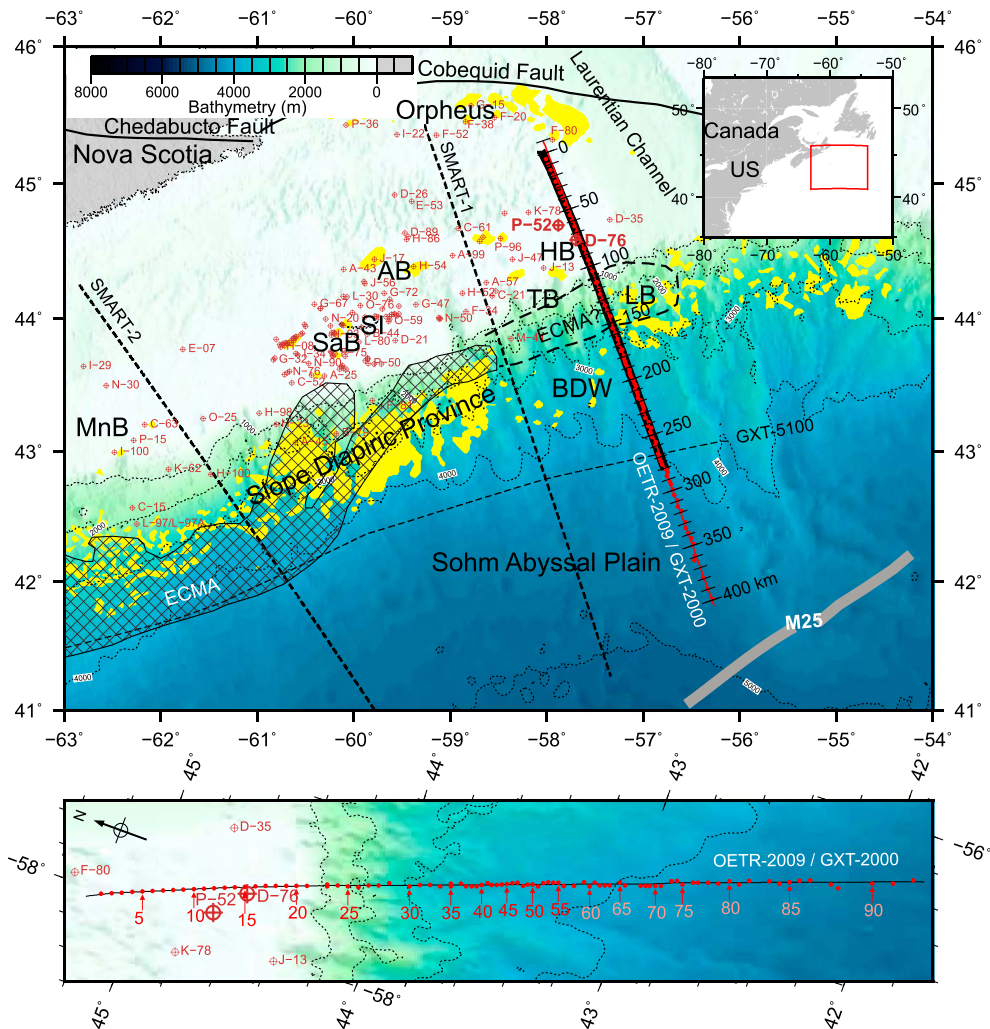
Figure 1. Bathymetry map (color scale) showing locations of the OETR-2009 ocean bottom seismometer (OBS) profile (red thin line is shooting profile and red dots are OBS locations), coincident MCS profile GXT-2000 (thick black line), SMART wide-angle seismic profiles (black thick dashed lines) (Funck et al., 2004; Wu et al., 2006), connecting MCS profile GXT-5100 (black thin dashed line) and selected boreholes (brown). The study area (red rectangle) is shown relative to eastern Canada and United States in the inset. The bathymetry is contoured (thin dotted lines) every 1,000 m. Yellow patches are salt (Shimeld, 2004). Diamond-patterned region is the East Coast Magnetic Anomaly (ECMA) with the black dashed curve outlining its recently proposed continuation (Sibuet et al., 2012). Thick gray line is the M25 magnetic anomaly. The OETR-2009 model distance is tick marked and labeled in black. Area around Profile OETR-2009 is enlarged in the lower panel with OBSs (red filled circles) numbered in red (pink on dark background), shooting line in black, and bathymetry contoured every 500 m. SI = Sable Island; MnB = Mohican Basin; SaB = Sable Basin; AB = Abenaki Basin; HB = Huron Basin; TB = Tantallon; LB = Laurentian Basin; DBW = Banquereau Detachment Wedge. MCS = multichannel seismic.

GmbH (Play Fairway Analysis Atlas, 2011). The much smaller OBS spacing on this profile than on the SMART profiles and the high definition of the crystalline basement available from the coincident GXT-2000 MCS line should allow for extraction of detailed crustal structural information, as was demonstrated by a recent similarly dense wide-angle profile collected just to the north in the Orphan Basin (Watremez et al., 2015). Based on a preliminary OETR-2009 velocity model, Luheshi et al. (2012) interpreted an anomalously high velocity crustal body within the COT as underplated material overlain by highly fractured basalt and, in conjunction with a reinterpretation of the SMART profiles, suggested that the magma-rich domain extends north up to the Newfoundland-Azores transform fault. This interpretation fundamentally changes our understanding of the tectonic setting of the margin, including the mechanism behind the transition from magmatic to amagmatic rifting.

In this paper, we analyze the OETR-2009 data set in its entirety using a layered velocity modeling method (Zelt & Smith, 1992), as applied for the SMART profiles, with the goal of detailing the COT found offshore northern Nova Scotia. In addition to providing comprehensive new information on the crustal structure of

the transected area, we address the debate on the general location of the transition from magmatic to amagmatic rifting offshore Nova Scotia. Understanding the complex crustal structure of the margin is also key in defining boundary conditions for petroleum system and salt tectonic modeling and plate reconstructions, which are used in assessing its hydrocarbon potential (Play Fairway Analysis Atlas, 2011). Finally, the high-resolution model for the OETR-2009 profile presented in this study allows for a detailed comparison with results from MIRROR-1, a recent OBS profile on the conjugate Morocco margin (Biari et al., 2015).

2. Geological Background

The Mesozoic rifting of Pangea that created the conjugate Nova Scotia and Morocco margins started in the Late Triassic (~230 Ma) and continued until the Early Jurassic (~175 Ma) (e.g., Klitgord & Schouten, 1986). Continental breakup then was followed by oceanic spreading to this day, which, despite the overall slow rate (e.g., Müller et al., 2008), formed a vast ocean basin with some of the oldest rifted margins in the world at its edges (Welsink et al., 1989). Both the Nova Scotia and Morocco continental lithosphere originally formed during the Paleozoic Appalachian Orogen. On the North American side of the Atlantic Ocean basin, the Cobequid-Chedabucto fault (Figure 1) separates the prerift Appalachian Orogen of Nova Scotia into the Meguma terrane (Williams, 1979), which comprises much of the Nova Scotia offshore, and the Avalon terrane found at the very northern end (Barr & Raeside, 1989). The high-amplitude (200–300 nT) ECMA, which can be explained by a synrift volcanic extrusive body in the southwestern part of the margin (Keen & Potter, 1995a), seemingly splits up into weaker (180 nT) and thinner lineations offshore central Nova Scotia and disappears further north, suggesting a loss of volcanic dominance (Dehler, 2012; Sibuet et al., 2012). The central Nova Scotia margin is potentially a tectonically complex zone equivalent to the conjugate Tafelney Plateau on the Moroccan margin. This region has been considered to be a transfer zone, formed by the juxtaposition of two detachment faults with dips of opposite polarity (Louden et al., 2013; Tari & Molnar, 2005).

The age of the onset of seafloor spreading is disputable but is believed to be somewhere between the age of the ECMA, which is itself disputable (190 Ma; Sibuet et al., 2012), and the M25 isochron (~155 Ma; Gradstein et al., 2004), which is the earliest identifiable magnetic anomaly of the margin (Figure 1). Using seismic constraints, Sibuet et al. (2012) interpreted an onset age of 177 Ma after a period of mantle exhumation, which is left entirely on the Canadian side by an eastward ridge jump, as no serpentinized mantle is observed on the Moroccan side.

Crustal thinning and subsequent sagging during the breakup created deep basins offshore Nova Scotia filled by up to 15 km of synrift and postrift sediment (Play Fairway Analysis Atlas, 2011). For our study area, the Scotian Basin beneath the outer shelf is subdivided into the Huron Subbasin, which is crossed by the OETR-2009 profile (Figure 1), and the Abenaki and Sable Subbasins to the southwest (Wade & Maclean, 1990). Further seaward, along the upper slope area, the OETR-2009 profile is situated within the Laurentian Subbasin, just northeast of its boundary with the Tantallon Subbasin (Play Fairway Analysis Atlas, 2011). Downdip, along the lower slope, the OETR-2009 profile crosses first into the Banquareau Detachment Wedge, which is a seaward section of the Tantallon Subbasin, before extending across what is possibly very thin oceanic crust (Funck et al., 2004). Only the outer shelf of the study area is well sampled by drilling (Figure 1). The subbasins in the study area were first filled by Triassic synrift red continental clastics and evaporites that later migrated seaward (Wade & Maclean, 1990), followed by postrift Early Jurassic clastics and carbonates (Play Fairway Analysis Atlas, 2011). Fully marine conditions that developed by Middle to Late Jurassic also deposited a thick succession of alluvial plain, deltaic, and carbonate facies, including the Abenaki carbonate bank, before more clastic and carbonate sediment continued to fill in the space produced by sagging. The thick sediments of the Laurentian Subbasin beneath the slope are extensively infiltrated by evaporites (the Slope Diapiric Province; Figure 1; Shimeld, 2004). No evaporites are, however, observed seaward beneath the Sohm Abyssal Plain where the COT is located (Funck et al., 2004).

3. Wide-Angle Seismic Data

Wide-angle seismic data were acquired along the 405-km-long OETR-2009 profile across the northeastern Nova Scotia margin (Figure 1). This margin normal OBS profile is located ~100 km to the east of the wide-angle seismic profile SMART-1 (Funck et al., 2004) and is coincident with MCS profile GXT-2000, which can be tied to the SMART profiles by margin-parallel Profile GXT-5100 in deep water (~4 km; Figure 1). The

OETR-2009 profile was defined along a great circle path, shot to coincide with the non-great-circle GXT-2000 profile, resulting in minor offsets. Data useful for analysis were recorded on 78 out of the 100 deployed OBSs, all with a sampling interval of 4 ms. Instrument spacing ranges from <3 km across the presumed COT (180- to 300-km model distance; Figure 1) to ~10 km at the seaward end of the profile (>360-km distance) and ~5 km for the remaining sections of the profile. Within each OBS, a group of three 4.5-Hz geophones (two horizontal and one vertical component) were mounted at the bottom of a glass sphere, which also housed the seismic recording unit. An external hydrophone was mounted to the top of the sphere. Only the vertical geophone and hydrophone data were used for the analysis presented in this work. An array of eight airguns (total volume of 64 L), towed at 10-m depth, was fired every 60 s to provide an average shot spacing of ~124 m.

Raw data were formatted into SEGY files for data analysis, which included noise attenuation, arrival picking, and velocity modeling. GeoPro GmbH supplied the standard timing corrections that account for gun delay (50 ms), a receiver specific constant time delay, and the OBS clock drift, all of which were applied to the data records. Gun positions were also corrected for the gun delay and the offset between the guns and the GPS antenna with uncertainties estimated to be well below that of the OBS positions. The OBS deployment positions were relocated to their seafloor positions, which were estimated by picking the direct water wave arrivals for each shot and ray tracing using a water velocity profile from a Conductivity Temperature Depth (CTD) cast by another survey nearby (42°33.88'N and 59°05.78'W). These corrected OBS and shot positions were then used to calculate the true source-receiver offset distances. A pick uncertainty of ±10 ms of the water arrival translates to a lateral uncertainty of 200- to 400-m depending on water depths (1.1–4.8 km). Note that the computed location errors represent the worst-case scenario in which all the pick errors are assumed to be either positive or negative. The root-mean-square (rms) misfits between calculated and observed arrival times translate to a horizontal position uncertainty of 8–300 m. OBSs shallower than 300 m were not relocated due to lack of clear water arrivals. The maximum normal distance between usable OBSs and shot profile is 1.0 km.

Common receiver gathers of OBS data were plotted, and coherent signals from compressional waves that underwent reflections and refractions (diving waves) through various seismic layers were picked. Figures 2–8 depict such OBSs records selected to show observations constraining key components of the modeled velocity structures. Unfiltered data were used for picking wherever possible. For deeper layers, band-pass filtering and predictive deconvolution were often necessary to improve the signal-to-noise ratio of the arrivals. Note that the filters used in the plots are optimized for the scale shown and not necessarily the ones used when picking.

3.1. Sediments

Figure 2 shows an example of refracted and reflected phases (Table 1) through the shallower sedimentary layers beneath the shelf. On the basis of their apparent velocity, we divide the observed sedimentary arrivals into three major groups belonging to the following sets of layers: shallowest layers (S1–S3) with phase (or apparent) velocities significantly lower than 4 km/s (the reduction velocity), deeper layers (S4 and S5) with phase velocity that is ~4 km/s, and the deepest layers (S6 and S7) that have much higher phase velocity than 4 km/s. The reflection from the top of Layer S4 is very strong throughout the profile, suggesting a large velocity discontinuity across the boundary. When the OBS record from Figure 2 is plotted using a greater offset range and higher-reduction velocity of 6 km/s (Figure 3), the rapid decrease and disappearance of the amplitude of the refracted phase through Layer S7 is observed at ~−22- and ~32-km offset distances (arrows in Figure 3), showing a phenomenon called step back. A step back in the first arrivals indicates a velocity inversion, which occurs wherever a layer of lower velocity is present underneath a layer of higher velocity (i.e., high velocity layer [HVL]). When rays penetrate the sub-HVL, they are refracted downward, creating a shadow zone. Layer S8 is, therefore, a sub-HVL. Neighboring OBS records from the shelf region also show a similar step back in the first arrivals. Since no returning rays can be observed from this layer, no direct velocity constraints are possible using refracted phases. However, the velocity of the sub-HVL is still weakly constrained by the moveout of the basement reflection and by assumption of continuity with adjacent sedimentary velocities on both sides. The wide-angle reflection from the top of Layer S8 and the offset distances at which the amplitude of the S7 refraction dies off constrain the thickness of Layer S7. No step backs are observed for refractions seaward of the shelf (e.g., Figure 4).

Underneath the slope at OBS 27 (Figure 4), the refracted phase of S6 is observed over a much wider offset range than landward, suggesting a dramatic thickening of this layer. The distortion in the shape of this
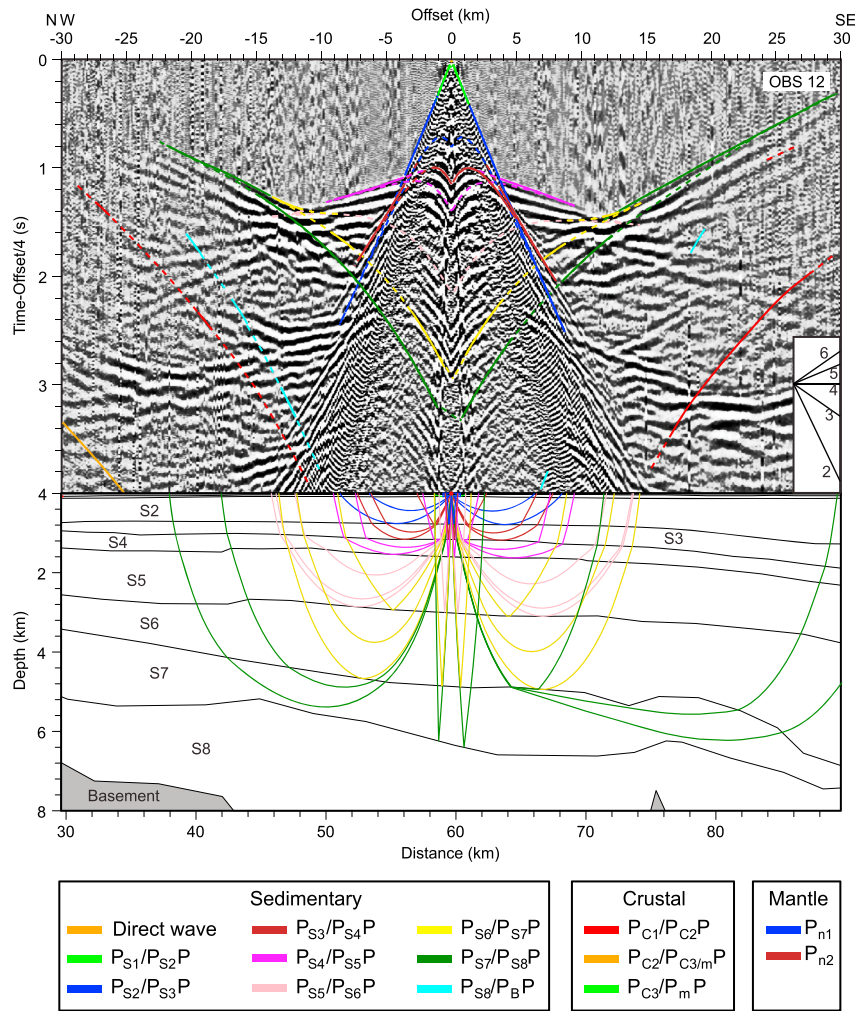
Figure 2. Velocity modeling of shallow sediments for OBS 12. Top: hydrophone data overlaid by theoretical traveltimes (color curves) versus model distances from ray tracing through the final velocity model. Dashed color segments are from forward modeling only, whereas solid segments are from two-point ray tracing. Traveltime is reduced by 4 km/s relative to shot-receiver offsets. The data have been processed with minimum-phase predictive deconvolution and band-pass filtering. Inset shows the linear moveout of different phase velocities in kilometer per second. Middle: the corresponding raypath diagram. Black lines are model boundaries, and gray areas are crustal layers. See legend (bottom) for color coding and Table 1 for nomenclature of the observed wave phases. OBS = ocean bottom seismometer.

phase also shows evidence of a salt diaper within this layer on the seaward side of OBS 27. Due to the rapid changes in water depth across the record, the observed phase velocities are not a good indication of the layer velocities. For example, arrivals for Layer S8 with phase velocity of ~4 km/s constrain much higher velocity of the deepest sediment above the basement. The phase for the layer above is sequentially numbered as S7 for simplicity although it has no resemblance to the same phase beneath the shelf landward where step backs are observed (Figure 3).

3.2. Crust and Uppermost Mantle

Figures 5–8 show OBS data that display velocity structures that uniquely define three crustal zones: continental (OBSs 3, 23, and 24), transitional (OBS 54) and oceanic (OBS 79). Regarding the continental crustal observations, OBS 3 (Figure 5) shows refracted and reflected arrivals (Table 1) from three layers (C1–C3) with phase velocities of 5–6 km/s. Refractions through Layers C1 and C3 both have relatively strong amplitudes, while the refraction through Layer C2 is weak, possibly due to scattering by the overlying complex structures. The wide-angle Moho reflection (P_mP) is normally of high amplitude at far offsets (>90 km) but can also be traced back to near offsets to constrain the depth of Moho beneath the thick crust (~12-s two-way traveltime [TWTT]).
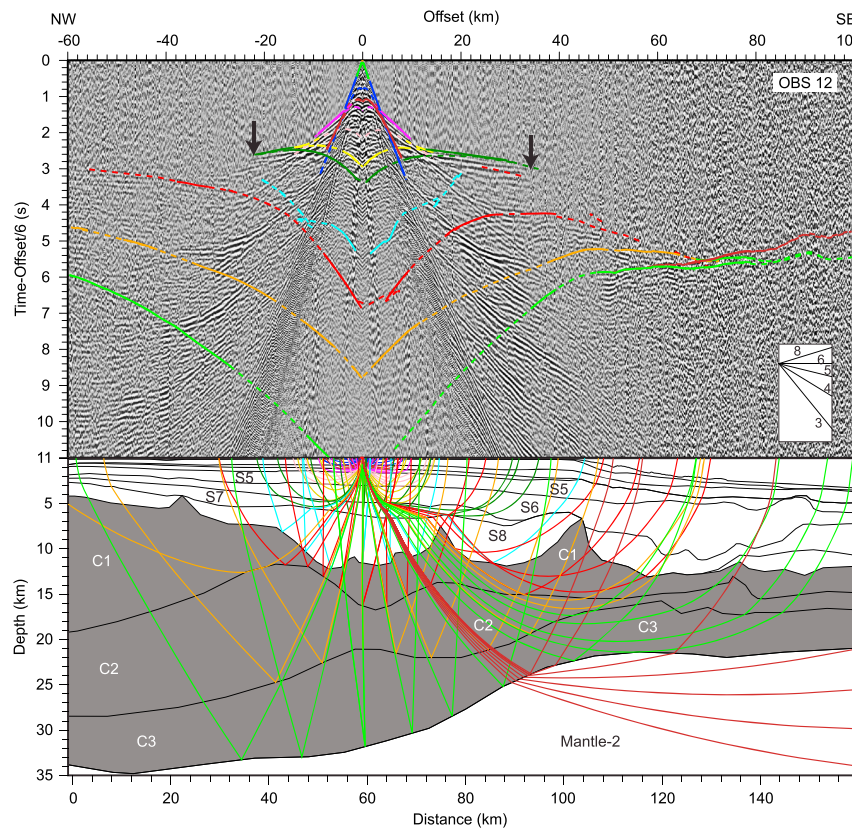
Figure 3. Velocity modeling of deeper sediments for OBS 12. Top: hydrophone data overlaid by theoretical traveltimes versus model distances from ray tracing through the final velocity model. Traveltime is reduced by 6 km/s relative to shot-receiver offsets. Black arrows show the beginning of a step back in arrival traveltimes. Bottom: the corresponding raypath diagram. Ray color legend is shown in Figure 2. Other information same as in Figure 2 caption. OBS = ocean bottom seismometer.

Figure 6 shows OBS records 23 and 24 with the crustal first breaks overall arriving later in time than the same arrivals at OBS 3 (Figure 5), especially at the right-hand side, which indicates basement deepening by crustal thinning in the seaward direction. The asymmetry between the two sides is mainly caused by the difference in seafloor depths (Figure 6). Unlike for OBS 3, the crustal refractions on the landward side of OBS 23 are poorly defined, possibly due to shadow zones caused by complex crustal structures. Nevertheless, the midcrustal and P_mP reflections are easily observed and constrain the crustal velocities. On the seaward side, the crustal arrivals recorded by OBS 24 appear distorted by the presence of a salt diaper at ~25- to 35-km offsets. The strong secondary arrivals of the C3 refraction provide the primary constraint for the velocity of this layer. Wide-angle midcrustal and Moho reflections also constrain the crustal thicknesses. Furthermore, with a gradual increase in phase velocities from one phase to another (deepest sedimentary phase velocity ~5 km/s, Layer C2 ~6 km/s, Layer C3 ~7 km/s, and mantle P_n ~8 km/s), the first arrivals form a moderately wide "U" shape.

The tighter the U shape, the thinner is the crust and in the extreme case, the first arrivals form a "V" shape as observed at the right-hand side of OBS 54 (Figure 7), which is located between the continental and the oceanic crustal zones. This unique pattern in the first arrivals defines our transitional crust. These waves only turn in the sediments (phase velocity ~5 km/s) and mantle (phase velocity ~8 km/s). This sharp contrast suggests the presence of extremely thin crust. The crustal refractions are only secondary arrivals and seemingly represent just an extended part of the Layer S8 refraction (light blue curve in Figure 7). Nevertheless, the existence of a very thin crust is supported both by the GXT-2000 coincident reflection image, which shows clear crystalline basement reflections at the top of Layer C1 in this area, and by strong P_mP reflections observed in the OBS data and arising at the crust-mantle boundary.

OBS 79 (Figure 8) is located seaward of the GXT-2000 profile within the oceanic crustal zone, where structures are probed only by the OETR-2009 profile. Despite the absence of a coincident MCS reflection image in this
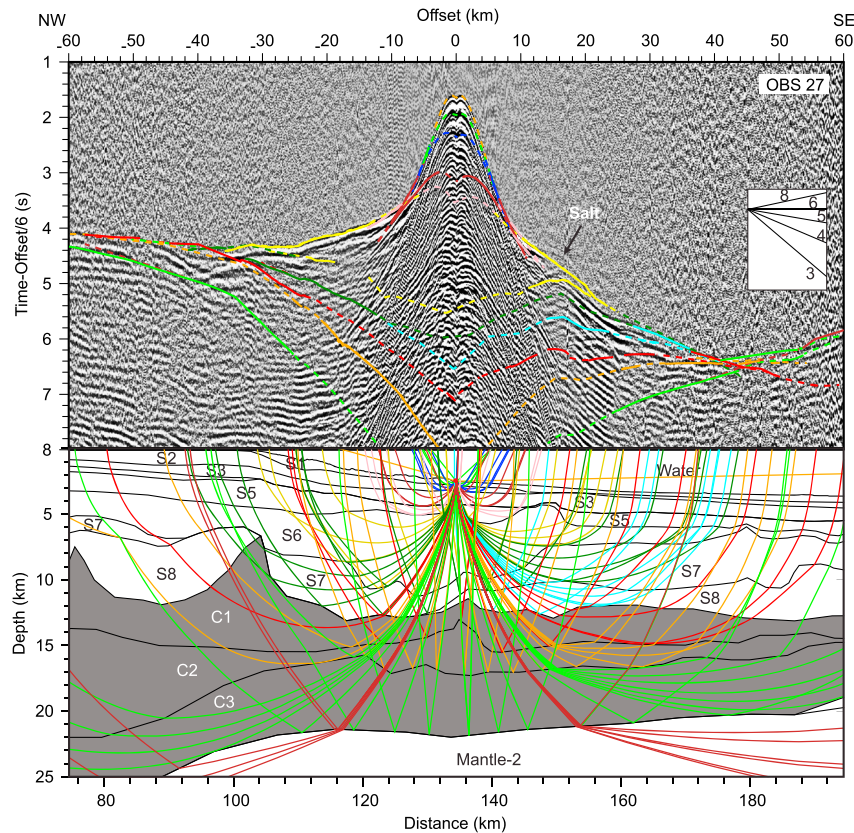
Figure 4. Velocity modeling for OBS 27. Top: vertical geophone data overlaid by theoretical traveltimes versus model distances from ray tracing through the final velocity model. Traveltime is reduced by 6 km/s relative to shot-receiver offsets. Bottom: the corresponding raypath diagram. Ray color legend is shown in Figure 2. Other information same as in Figure 2 caption. OBS = ocean bottom seismometer.

area, geometry of the structural boundaries is well constrained because we observe numerous high-amplitude wide-angle reflections in the OBS data. The most prominent sedimentary reflection in the OBS data comes from the top of Layer S7, suggesting a large velocity discontinuity (a transition from ~3 to ~4 km/s) across the boundary. The base of Layer S7 (the basement reflection; dark green in Figure 8) is also clearly observed and constrains the depth and topography of the crust. The phase velocity of the refracted Phase L2 (~5 km/s) is mostly a result of changes in basement topography. The refracted Phase L3 is affected by distortions caused by the basement topography, as well as that of the midcrustal boundary. However, L3 forms first arrivals that are distinguishable from those of the upper crustal Layer L2, supporting a two-layered oceanic crustal structure. The amplitude of Phase L3 dies off abruptly before the mantle phase (P_{n2}) indicating a large decrease in velocity gradient, as amplitude is proportional to velocity gradient. However, the apparent velocity of Phase L3 increases gradually toward the bottom of this layer (larger offset distances) and transitions smoothly to P_{n2}, suggesting a minor velocity discontinuity with the mantle. Weak and intermitted appearances of P_mP can be observed and constrain the depth to Moho. Overall, this record section and those from nearby OBSs show very different velocity structure than the ones found landward (Figures 1–7).

For the deepest phases, strong leftward dipping first arrivals with a phase velocity of >7 km/s (P_{n1} for Layer Mantle-1) are observed at 26- to 44-km offset distances on OBS 54 (Figure 7). Such a high phase velocity is unlike those observed for normal continental and oceanic lower crust (cf. P_{C3} of OBS 24 in Figure 6 and P_{C2} on OBS 79 in Figure 8). The P_{n1} phase is observed to be continuous in dip with that of the P_{n2} phase from the deepest layer at the far offset distances without a wide-angle reflection, suggesting no velocity contrast across the two phases. Therefore, the P_{n1} phase is likely to come from the mantle or an area that consists to some degree of mantle rocks. This indicates very thin (~4 km) crust for the region sampled by OBS 54. The sharp decrease in amplitude across the two phases (~44-km offset) further signifies a large discontinuity in
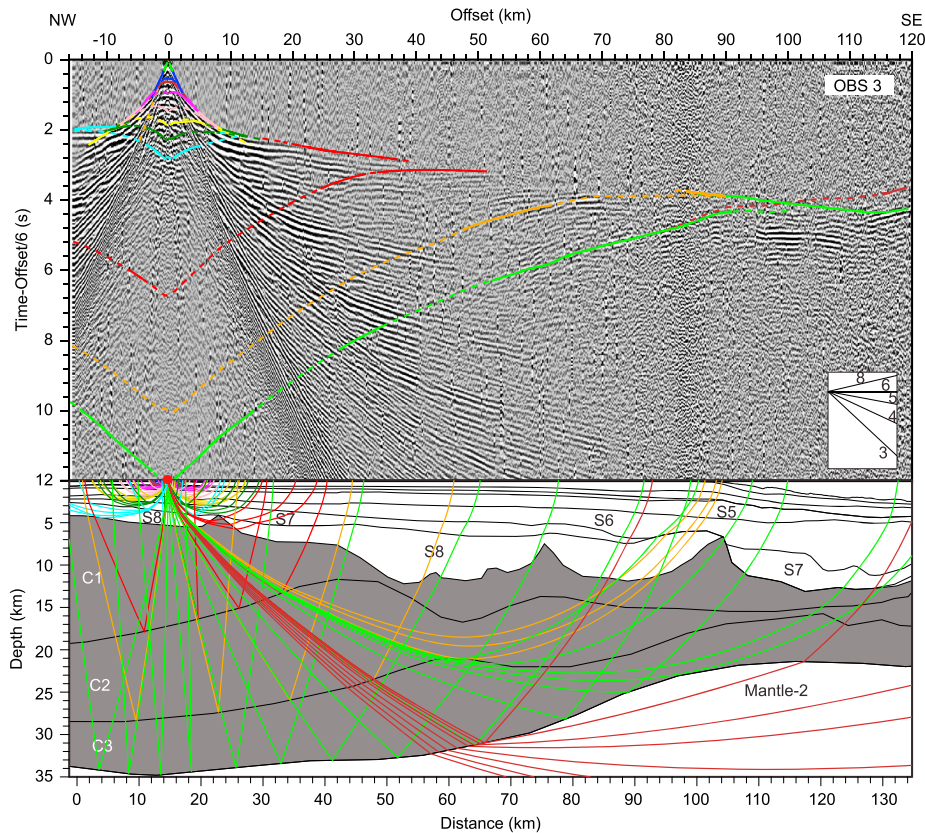
Figure 5. Velocity modeling for OBS 3. Top: hydrophone data overlaid by theoretical traveltimes versus model distances from ray tracing through the final velocity model. Traveltime is reduced by 6 km/s relative to shot-receiver offsets. Bottom: the corresponding raypath diagram. Ray color legend is shown in Figure 2. Other information same as in Figure 2 caption. OBS = ocean bottom seismometer.

velocity gradient. The P_{n2} phases with a phase velocity of ~8 km/s are well observed along the profile (Figures 3–8), except for the two ends where offsets are restricted. Its low amplitude and frequency are characteristics of normal, unaltered mantle. The arrival times of P_{n2} also provide an important constraint on Moho depth (Figures 3–8).

4. Seismic and Gravity Modeling

4.1. Methodology

We use RAYINVR, the ray tracing algorithm of Zelt and Smith (1992), to model the *P* wave velocity by fitting the seismic arrival traveltimes layer by layer in a top-down approach. Seafloor depths are determined using the TWTTs projected from the MCS profile GXT-2000 (Figure 1) converted to depths by a constant water velocity of 1.5 km/s. For seafloor depths at the seaward end of the OETR-2009 profile (south of OBS 71) not covered by GXT-2000 profile, we use the GEBCO_08 grid (General Bathymetric Chart of the Oceans, 2008). For consistency, these depths were first converted to TTWTs using an estimated water velocity profile from a nearby CTD cast and then back into equivalent depths for 1.5-km/s water velocity. Although constraints for velocity modeling of the subbottom layers come from OBS data, this modeling process is also informed by the layer boundary locations from the coincident GXT-2000 MCS reflection image.

The fitting of forward modeled traveltime curves to observed arrival times was initially done visually for the purpose of phase identification (Figures 2–8). Once a complete preliminary model was produced, the zero-crossing times of identified phases were handpicked with each pick assigned an uncertainty value based on the frequency content and signal-to-noise ratio of individual wavelets (Table 2). These picks were then used for inverse modeling to form an optimally fitted final model. Due to the large numbers of phases identified from the data, we screened out 65 OBS stations that have good data quality and provide an even distribution of observations along the profile for picking (red stars; Figure 9). Picks were subsequently
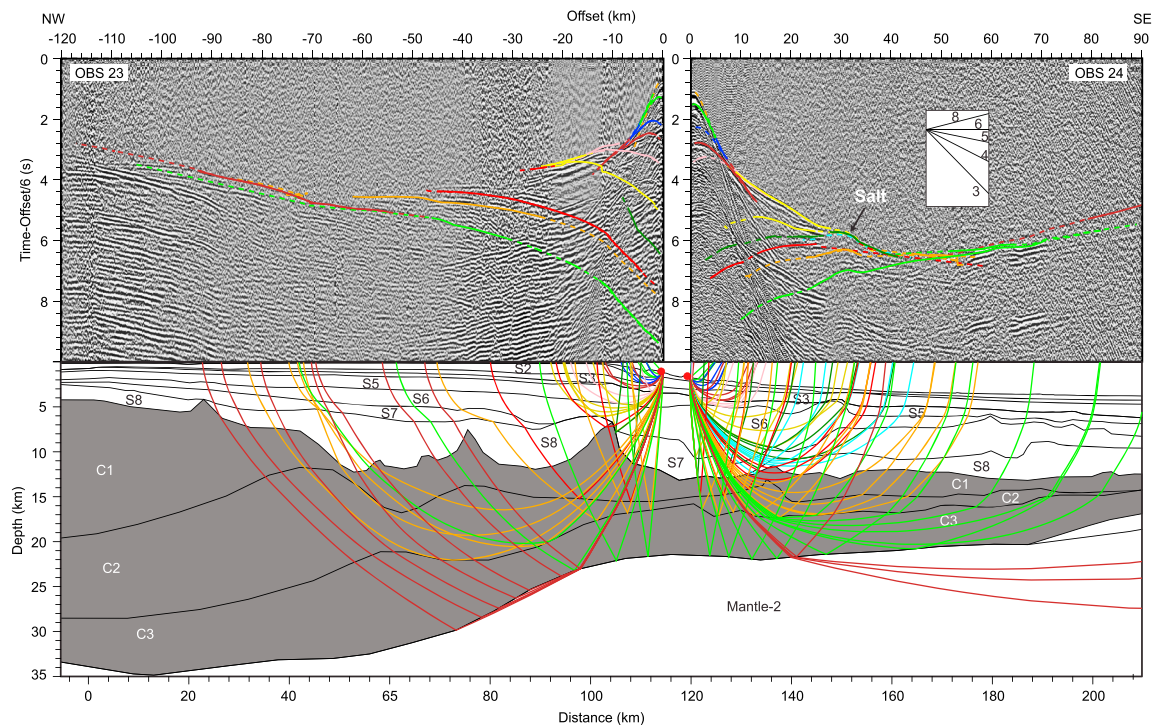
Figure 6. Velocity modeling for OBS 23 (left) and 24 (right). Top: vertical geophone (OBS 23) and hydrophone (OBS 24) data overlaid by theoretical traveltimes versus model distances from ray tracing through the final velocity model. Traveltime is reduced by 6 km/s relative to shot-receiver offsets. Bottom: the corresponding raypath diagram. Ray color legend is shown in Figure 2. Other information same as in Figure 2 caption. OBS = ocean bottom seismometer.

decimated to obtain a minimum pick interval of 100 m to avoid overweighting regions densely populated with data traces in the inversion and error analysis. The original trace spacing is less than 100 m in the near-offset region of OBSs not positioned right on the shot line, as well as where parts of the profile were reshot.

4.2. *P* Wave Velocity Model

Figure 9 shows the final *P* wave velocity model as well as the density of refracted and reflected rays used in the inverse modeling. For a detailed comparison with well data and previous velocity models, 1-D profiles are extracted at key locations and shown in Figures 10 and 11.

The modeled sedimentary velocities are generally consistent within the layers across the profile with the exception of a limited extent in Layers S6 and S7 beneath the shelf (0- to 100-km model distances; Figure 9a). Layers S1–S3 are the youngest sedimentary layers whose velocities of 1.7–2.9 km/s are substantially lower than the velocities of the deeper layers as shown by their moveouts in Figure 2. The largest velocity jump (~1.2 km/s) across the bottom boundary of Layer S3 is modeled beneath the shelf where two wells are located nearby and the carbonate Wyandot formation is drilled at similar depths (P-52 and D-76; BASIN Database Team, 2017; Figures 9a and 10). The OBS data require that Layer S4 is modeled with higher velocity than measured by downhole seismic in the wells (Wyandot formation). A small velocity inversion at the top of Layer S5 is also needed to model a minor step back in the OBS data (Figure 2). This minor velocity reduction is also suggested by the well data (Figure 10). Top of Layer S6, characterized by a small step velocity increase, coincides with the O-Marker within the Mississauga formation at well P-52. The O-Marker is a high-amplitude reflector at the top of a series of thin transgressive limestone beds of Hauterivian to Barremian age (Barss et al., 1979; Jansa & Wade, 1975). Beneath this boundary, velocities increase steeply into the Mic Mac and Baccaro formations to reach ~5.8 km/s at the top of Layer S7 at distances 60–90 km. Velocities in Layer S7 are vertically nearly uniform (i.e., show a low gradient). Beneath these high velocities, a low-velocity zone (S8; 4.7–5.4 km/s) exists within two subbasins at distances ~25–105 km (Figures 9a and 10). The velocities of 5.3–5.8 km/s at the landward end of Layer S8, however, approach those of the upper crust (Figure 9a).
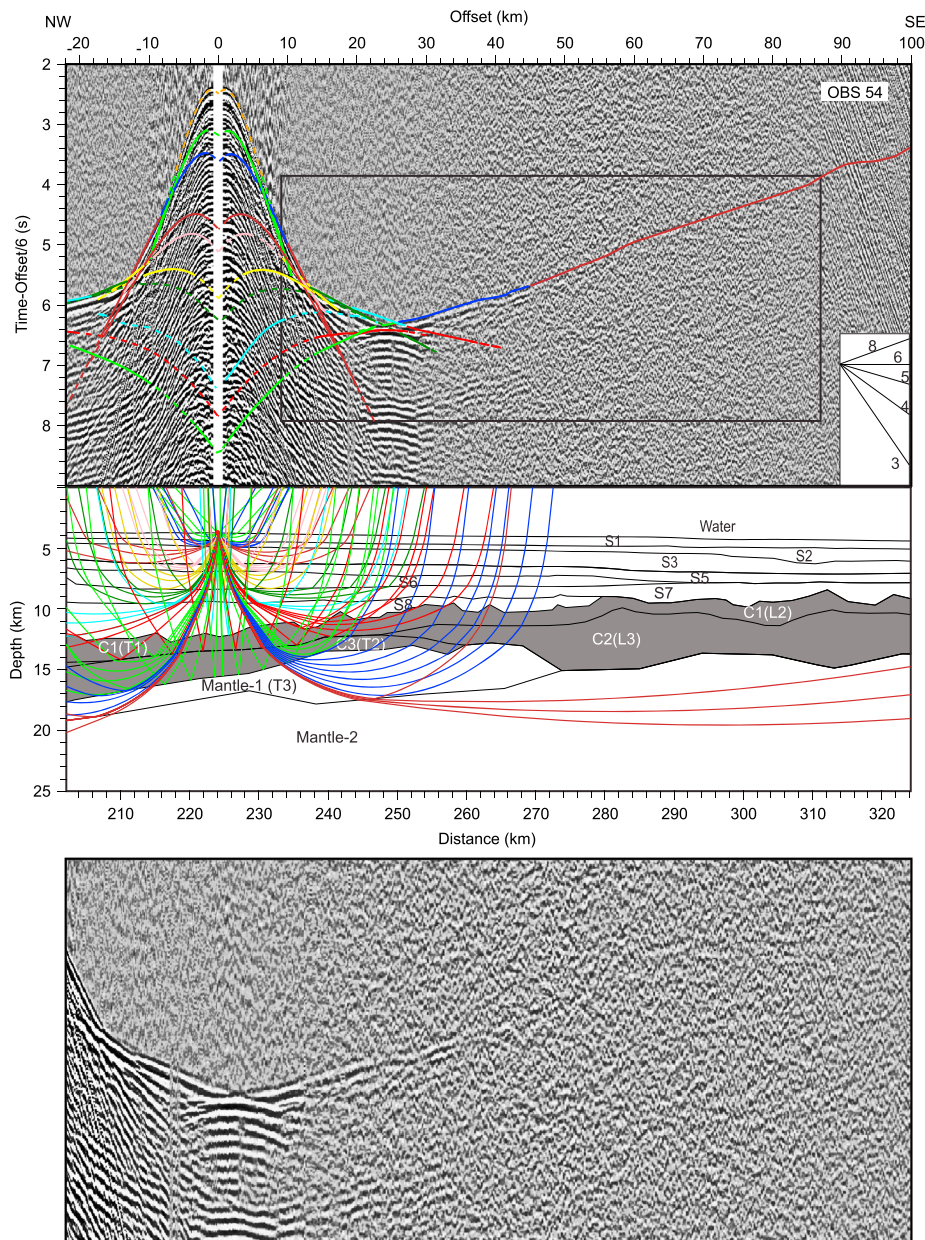
Figure 7. Velocity modeling for OBS 54. Top: vertical geophone data overlaid by theoretical traveltimes versus model distances from ray tracing through the final velocity model. Traveltime is reduced by 6 km/s relative to shot-receiver offsets. Data within the black rectangle are plotted at the bottom without the traveltime curves to show details of the crustal and mantle arrivals. Middle: the corresponding raypath diagram. Ray color legend is shown in Figure 2. Other information same as in Figure 2 caption. OBS = ocean bottom seismometer.

Seaward beneath the slope, lateral heterogeneity that mimics salt diapiric structures is modeled within Layer S6 (Figure 9a). This layer reaches a maximum thickness of ~6 km at 128-km distance, seaward of which both its thickness and velocity decrease until it pinches out at 293-km distance. The velocity of Layer S7 is highest (4.8–5.2 km/s) at the slope where the overburden is thickest but decreases to a minimum of 3.7 km/s at the seaward end where the overburden is thinner. The otherwise smooth top boundary of S7 is distorted into highs by modeled salt structures at several locations, indicating that salt tectonics occurred after the deposition of this sedimentary package. Layer S8, the deepest sedimentary layer, has velocities of 4.8–5.3 km/s and pinches out onto the basement at 295-km distance.

Crustal layers C1–C3 are modeled with velocities of 5.0–7.4 km/s, which are generally higher than velocities for most sediments (Figures 9a and 10). The top boundary of Layer C1 is constrained by the interpreted
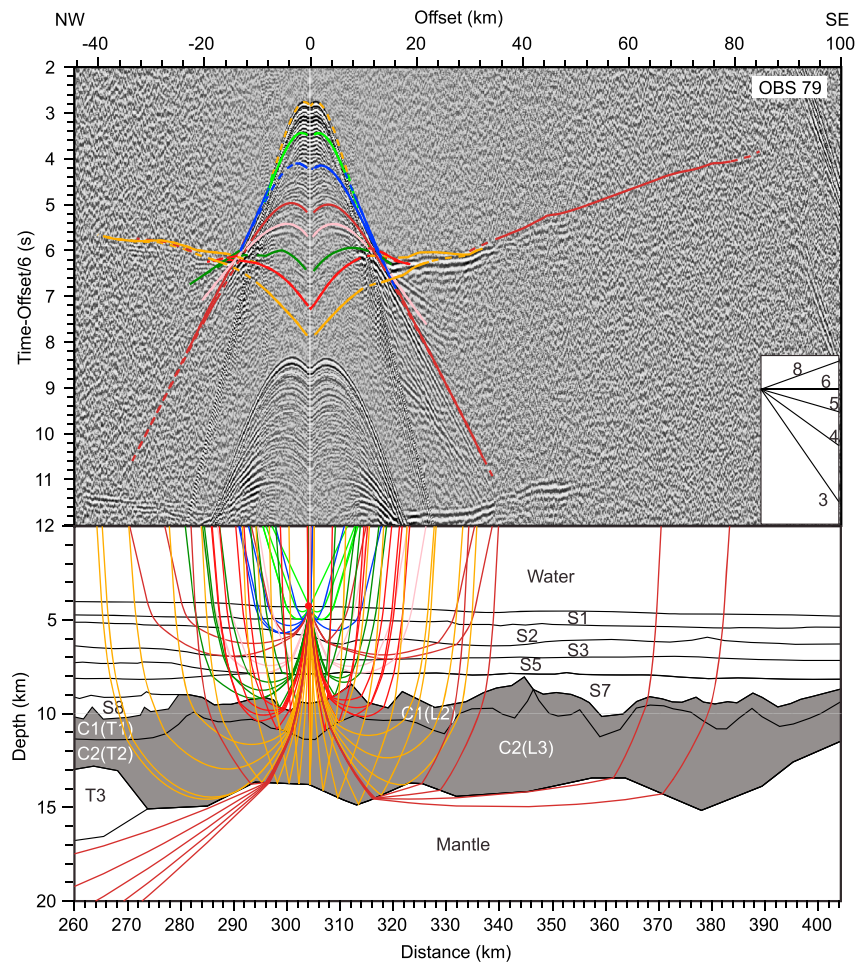
Figure 8. Velocity modeling for OBS 79. Top: hydrophone data overlaid by theoretical traveltimes versus model distances from ray tracing through the final velocity model. Traveltime is reduced by 6 km/s relative to shot-receiver offsets. Bottom: the corresponding raypath diagram. Ray color legend is shown in Figure 2. Other information same as in Figure 2 caption. OBS = ocean bottom seismometer.

basement reflection from the coincident MCS profile. The crustal layers also display two horizontal transitions in velocity indicating three distinctive crustal zones: continental (C), transitional (T), and oceanic (L; Figure 9a). Some of these lateral transitions resulted in pinching out of layers in the model as shown in Figure 9a, while others did not require an actual boundary (i.e., velocity step) in the model.

Table 1
Glossary of Seismic Phases

Phase	Description
Direct	Direct wave through the water
P_{sn}	*P* wave refracted phase through the *n* sedimentary layer from the top
$P_{sn}P$	*P* wave reflected phase from the bottom of the *n* sedimentary layer from the top
$P_{s6}P$	*P* wave reflected phase coincident with the interpreted "O-Marker"
P_{s7}	*P* wave refracted phase through interpreted carbonate layer beneath the shelf
P_BP	*P* wave reflected phase from the basement top
$P_{C1}/P_{C2}/P_{C3}$	*P* wave refracted phase through the upper/middle/lower crystalline crust
$P_{C2}P/P_{C3}P$	*P* wave reflected phase from the top of the middle/lower crystalline crust
P_mP	*P* wave Moho reflection or reflection at the crust-mantle boundary
P_{n1}	*P* wave refracted phase through interpreted, serpentinized mantle (T3)
P_{n2}	*P* wave refracted phase through normal mantle

Table 2
Error Analysis Statistic for Picked OBSs

	Phase	n	Mean $t_{uncertainty}$ (s)	t_{rms} (s)	χ^2
Sediment	P_{S1}	658	±0.018	0.029	2.861
	$P_{S2}P$	3092	±0.021	0.018	0.791
	P_{S2}	2980	±0.017	0.025	2.304
	$P_{S3}P$	4407	±0.024	0.027	1.192
	P_{S3}	5553	±0.029	0.043	1.706
	$P_{S4}P$	9394	±0.032	0.034	1.157
	P_{S4}	822	±0.023	0.020	0.737
	$P_{S5}P$	338	±0.025	0.023	0.789
	P_{S5}	3185	±0.033	0.041	1.708
	$P_{S6}P$	6952	±0.033	0.030	0.799
	P_{S6}	4410	±0.037	0.060	2.714
	$P_{S7}P$	4514	±0.043	0.061	1.879
	P_{S7}	7271	±0.042	0.045	1.131
	$P_{S8}P/P_BP$	7223	±0.046	0.062	1.566
	P_{S8}	2739	±0.048	0.051	1.166
	$P_{B'}P$	4567	±0.049	0.059	1.404
Crust	P_{C1}	3598	±0.049	0.052	1.080
	$P_{C2}P$	11387	±0.060	0.113	2.967
	P_{C2}	7135	±0.053	0.068	1.700
	$P_{C3}P/$ $P_{m'}P$	9278	±0.061	0.090	2.055
	P_{C3}	5186	±0.069	0.148	4.191
	P_mP	13805	±0.083	0.163	3.805
Mantle	P_{n1}	1726	±0.050	0.051	1.260
	P_{n2}	14937	±0.087	0.174	3.394
All		135157	±0.053	0.099	2.177

Note. The number of raytraced picks (n), mean uncertainty of all input picks ($t_{uncertainty}$), rms residual between modeled and observed traveltimes (t_{rms}), and normalized (χ^2) are shown for each individual phase and all the phases together. The basement reflection is comprised of P_BP (reflection from the bottom of S7 where S8 is absent) and $P_{B'}P$ (reflection from the bottom of S8). P_mP (reflection from the bottom of C3) is the continental Moho, whereas $P_{m'}P$ (reflection from bottom of L3) is the oceanic Moho. OBS = ocean bottom seismometer. rms = root-mean-square.

The full-thickness (~30 km) continental crust modeled at the landward end of the profile is comprised of three subcrustal layers based on their distinctive velocity structures (Figures 9a and 11a). The upper crust (C1) has the highest gradient (0.04/s), the lowest velocities (5.6–6.3 km/s), and the largest thickness (16 km); the middle crust (C2) shows intermediate gradient (0.02/s), velocity (6.4–6.6 km/s), and thickness (9 km); and the lower crust (C3) has the lowest gradient of 0.01/s, the highest velocities (6.9–7.0 km/s) and the smallest thickness (5 km). While the crust as a whole does not thin until seaward of 22-km distance, the upper crust first thins gradually starting from the landward most end followed by abrupt thinning to ~1-km seaward at ~52-km distance (Figure 9a). In contrast, both the middle and the lower crustal layers thicken slightly seaward from the landward end of the profile to a thickness of 13 and 11 km, respectively, before rapidly thinning seaward to 4 km at 60- and 80-km distances, respectively. The velocity gradient increases seaward as the crustal layers thin, with the largest increase modeled within the middle crust, while the velocities decrease (upper crust ~5.3–6.1 km/s, middle crust ~5.7–6.5 km/s, and lower crust ~6.5–6.8 km/s) in the same direction. Local thickening of the upper and middle crust occurs seaward of the hinge zone found at ~35- to 60-km distance, suggesting the presence of tilted fault blocks. The seaward thinning, followed by thickening, of the lower crust seaward of the hinge zone is, in contrast, more regional, gentle, and smooth. Seaward, toward the limit of the continental zone (140–172 km), the velocity structures change slightly: the lower crustal velocity gradients decrease to 0.04–0.06/s and the corresponding velocity increases to >7 km/s. As the Moho forms a concave downward geometry seaward of distance 70 km, numerous rays diving in both directions through the mantle (Figure 9b) can be observed and a normal mantle velocity of 8.0 km/s is modeled.

The transitional zone (172–272 km) farther seaward clearly shows a very different set of velocity structures (Figures 9a, 11b, and 11c). Layer T1, the transitional zonal equivalence of Layer C1, has both very low velocity (5.3–5.4 km/s) and velocity gradient (lowest ~ 0.04/s) toward the middle of the zone but a more-or-less constant thicknesses of ~1–2 km (Figure 9a). The middle crust (C2) pinches out within this zone, creating a large velocity discontinuity across the boundary between Layers T1 and T2 (the transitional zonal equivalence of Layer C3; velocities ~6.3–7.5 km/s). Layer T2 also thins seaward from a thickness of 4.7 km until pinching out at ~260-km distance, while its velocity gradient increases to a maximum of 0.6/s at distance 236 km, which is abnormally high for crustal layers (Figures 9a and 11a–11c). Underneath Layer T2, a new Layer T3 is modeled with a velocity structure that is very different from other modeled layers. Its velocities of 7.1–8.0 km/s are approximately in between those of the Layer C3/T2 landward and normal mantle underneath. Therefore, the velocity discontinuity across Layers T2 and T3 is small (~0.5 km/s) at the landward and seaward ends (Figure 11c), and no velocity discontinuity into the underlying normal mantle layer at distance 221 km is modeled (Figure 11b). Layer T3 also has a relatively high velocity gradient of 0.16–0.42/s (Figures 9a, 11b, and 11c) and a general seaward increase in thickness to a maximum of 4.3 km at distance 240 km (Figures 9a and 11c) before it steeply thins and pinches out seaward into the oceanic zone.

The other major lateral change in velocity structures is modeled seaward, from the transitional to the oceanic zone (Figure 9a). The basement in the oceanic domain is elevated to ~9- to 10-km depth and is characterized by rough topographic highs. Layer L2, which is modeled as an extension of C1/T1 that we interpret as oceanic Layer 2, is highly variable in velocity (5.0–5.9 km/s), velocity gradient (0.1–0.5 s), and thickness (0.4–1.9 km/s) across this zone. The midcrustal boundary at the base of oceanic Layer 2 is equally rough and marks a high velocity discontinuity into oceanic Layer 3 (L3) with modeled velocities of 6.2–7.4 km/s (Figures 9a and 11d). The modeled velocity gradient is consistently high (~0.25/s) across L2 and L3. Despite the large variations in
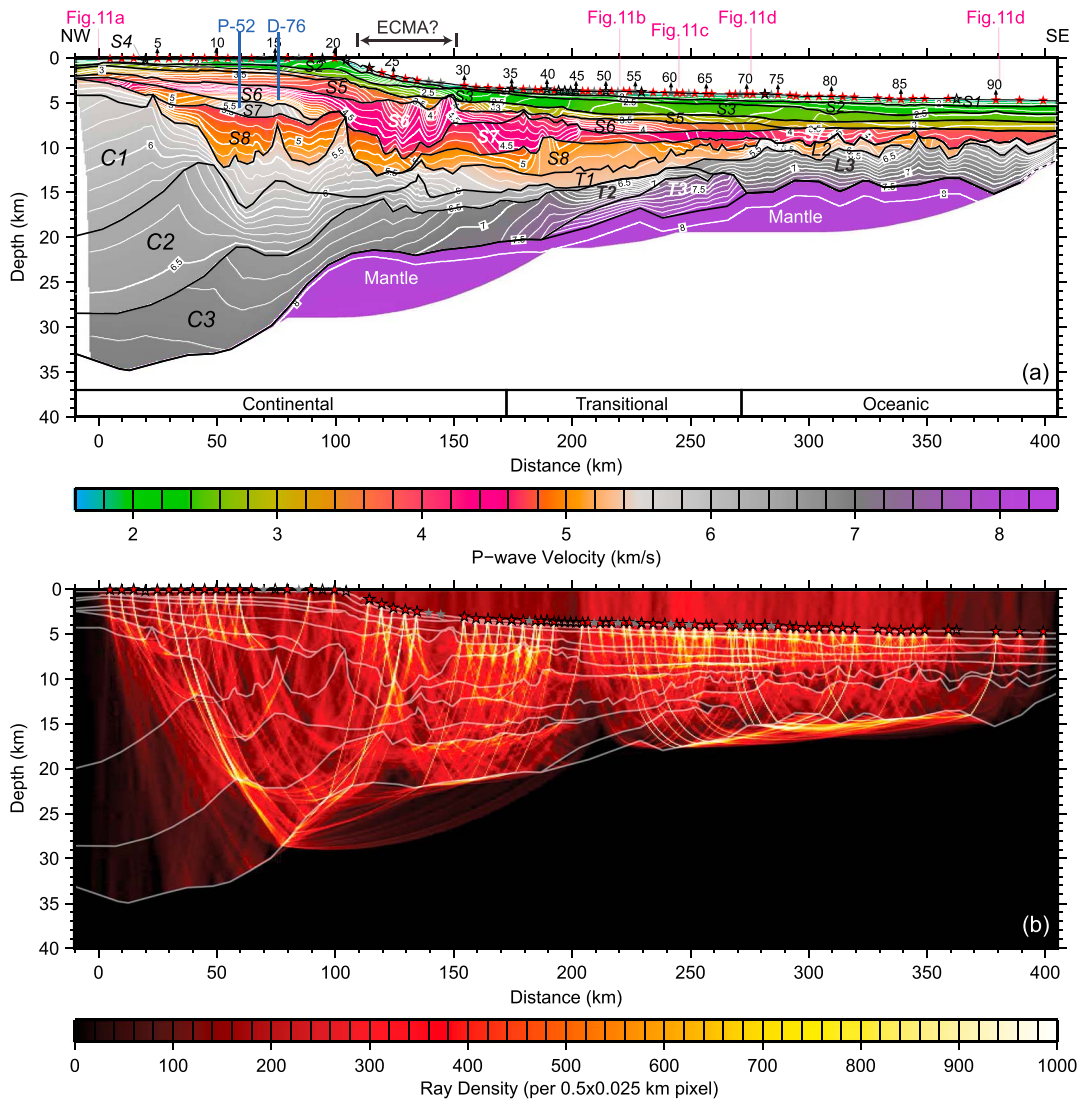
Figure 9. Final *P* wave velocity model of the OETR-2009 profile (a) and constraining ray diagram (b). (a) Stars are OBS locations with filled colors representing differing constraints input to the model: red, fully picked; gray, not picked; unfilled, no data. The velocity model has layer boundaries in black lines and velocities defined by color scale. Dashed line segment of Moho boundary at the right-hand model end is different from that of the density model in Figure 13. Layers are labeled according to Figure 2 legend and Table 1 except that C1–C3 are replaced with T1-T2 and L2-L3 for the transitional and the oceanic zone, respectively. White rectangles at the bottom show crustal zonal interpretations (see text). Velocities are contoured every 0.1 km/s (white lines). OBS numbers are above black arrows; vertical blue lines are well positions projected along profile. Vertical pink lines locate the 1-D velocity–depth profiles plotted in Figure 11. Area outside of ray coverage is masked. ECMA = extent of possible northeastward continuation of the East Coast Magnetic Anomaly (Sibuet et al., 2012). (b) Illumination diagram showing ray density in color (truncated at 1,000 rays/0.5 × 0.025-km pixel). Only rays used for inversion are shown. Gray lines are model boundaries. OBS = ocean bottom seismometer.

both the top and bottom boundary depths, the thickness of the Layer 3 remains relatively consistent at ~3.7 km, except at the seaward end (>390-km distance) where it is thinner, although the modeling constraints are poor at the model edges. A normal mantle velocity of 8.0 km/s is modeled beneath Layer 3 (Figure 9a).

4.3. Error Analysis and Resolution for Velocity Model

We performed statistical error analysis (Table 2) of our final velocity model (Figure 9a) by calculating the rms residual t_{rms} (0.10 s overall) and normalized χ^2 (2.18 overall), with respect to their pick uncertainties (10–150 ms). When χ^2 is ~1, observed data are neither overfitted nor underfitted by the model, which is considered optimal. However, complexities in modeled structures such as large tilted fault blocks, salt diapirs, and velocity inversions across rifted margins as in our case (e.g., Funck et al., 2004; Lau et al., 2006) commonly cause the ray tracing algorithm to fail for a number of picked arrivals, making χ^2 of ~1 impractical.
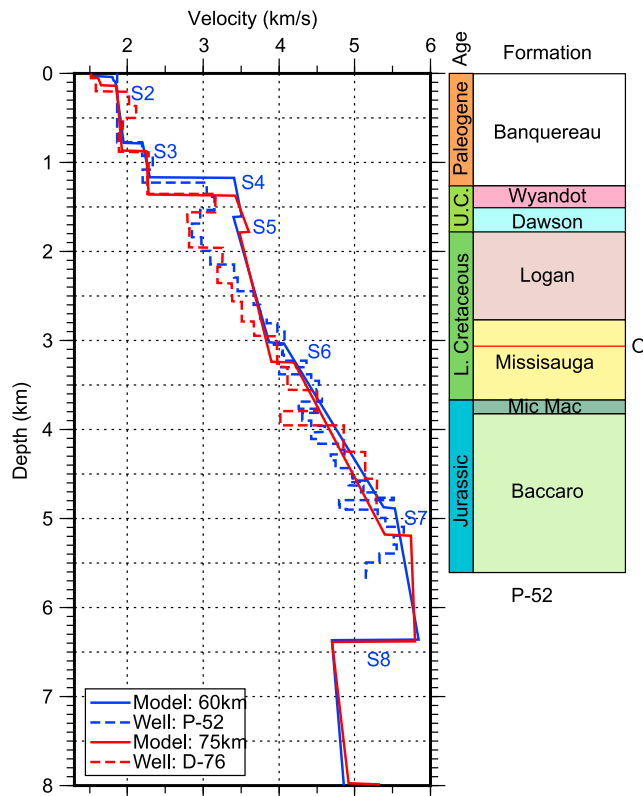
Figure 10. One-dimensional velocity versus depth profiles through the sedimentary layers of the final model at 60- and 75-km model distance (solid lines) shown together with projected locations of wells P-52 and D-76, respectively, and their corresponding downhole seismic models (dashed lines). Layers are labeled for model at 60 km according to Figure 9a. Ages and depths of stratigraphic formations and location of the O-marker (red line) are taken from previous interpretations of well P-52 (BASIN Database Team, 2017).

According to Table 2, half of the 24 inverted phases have a $\chi^2 \leq 1.5$ and three quarters have a $\chi^2 \leq 2$. For the remaining quarter of phases, two of which are sedimentary (P_{s1}, P_{s6}), three crustal ($P_{c2}P$, P_{c3}, and P_mP), and one mantle (P_{n2}), χ^2 is >2.5. The larger value for P_{s1} (2.86) is a combination of an oversimplification of complex seafloor velocity structures and small pick uncertainties (mean = ±0.02 ms) due to high signal-to-noise ratio of the arrivals. For P_{s6}, its χ^2 value of 2.71 is likely due to the blending of the steeply dipping salt structures in Layer S6 and the surrounding sediment into a single layer (Figure 9a). Wide-angle crustal reflections also tend to have worse fits than those of the sediment due to multipath diffractions caused by rough layer interface geometry such as those of $P_{c2}P$ and P_mP (Figure 5) within the continental zone and larger uncertainties in their interpretations not included in the error analysis. Furthermore, the large χ^2 of P_{c3} and P_{n2} stems from the impossibility of detailed fitting of a deep layer across many OBSs that sampled the same region, as misfits are compounded from shallower layers and their large traveltimes also mean that only a small percentage in error will translate into a large χ^2.

The resolution for different parts of the model is represented by the diagonal values of the resolution matrix (Zelt & Smith, 1992) for each velocity (Figure 12a) and depth node (Figure 12b). The resolution matrix values can range from 0 to 1 and are controlled by the number of picks and their distribution in relation to the structures. Regions with resolution >0.5 have relatively better resolution and vice versa. Regarding the velocity resolution, starting from the sedimentary layers, most parts of the top-most sedimentary layers (S1–S3) are well resolved (>0.7; Figure 12a). The deeper sedimentary layers (S5–S8) have relatively good resolution beneath the slope and seaward. The thickest parts of the sedimentary Layers S6 and S7 where salt structures are present (125–140 and 160–190 km, respectively) are among the best resolved. For the continental crust, all three crustal layers are relatively well resolved beneath the shelf away from the landward end of the model, and Layers C1 (upper crust) and C3 (lower crust) remain well resolved underneath the continental rise. The transitional Layers T1 and T3 show fairly high resolution at distance 240–265 km. The oceanic Layer 3 (L3) is also relatively well resolved landward of 350-km distance. With resolution >0.9 over two major regions that are sampled by a large number of rays, the normal mantle layer is the best resolved layer of the model (Figures 9b and 12a). Resolution at the two ends of the model and at pinch outs of layers is often poor due to the lack of constraining rays. Other locations of moderately poor resolution (<0.3) include Layers S4–S7 for distances 50–100 km (but they are also constrained by boreholes; Figure 10) and Layers L2 and T2 where velocity gradients are high within relatively thin layers. Another reason for low resolution is the large gap in instrument spacing between OBSs 41 and 46 and between OBSs 89 and 90. Finally, the shadow zone created by the velocity inversion at the top of Layer S8 under the shelf also resulted in poor resolution within the basin (distance 70–105 km).

The resolution of the depth nodes (Figure 12b) is predominantly high (>0.7) as most of the boundaries are sampled by reflected phases (black lines in Figure 12a). Low resolution is only present at a few locations where no reflections from the boundaries can be observed (white lines in Figure 12a). Note that unreflective model boundaries, such as the base of Layer T3, are created only for the purpose of changing the vertical velocity gradients within what would otherwise be a single continuous velocity layer.

4.4. Gravity Modeling

By using the velocity-to-density conversion curve shown in Lau et al. (2006) and the methodology of Talwani et al. (1959) and Won and Bevis (1987), we construct a 2-D gravity model that corresponds to the velocity structures in our final velocity model. This gravity model is then compared with the observed satellite gravity (Figures 13a and 13b; rms misfit = 4.0 mGal; Sandwell et al., 2014). The density model extends with uniform
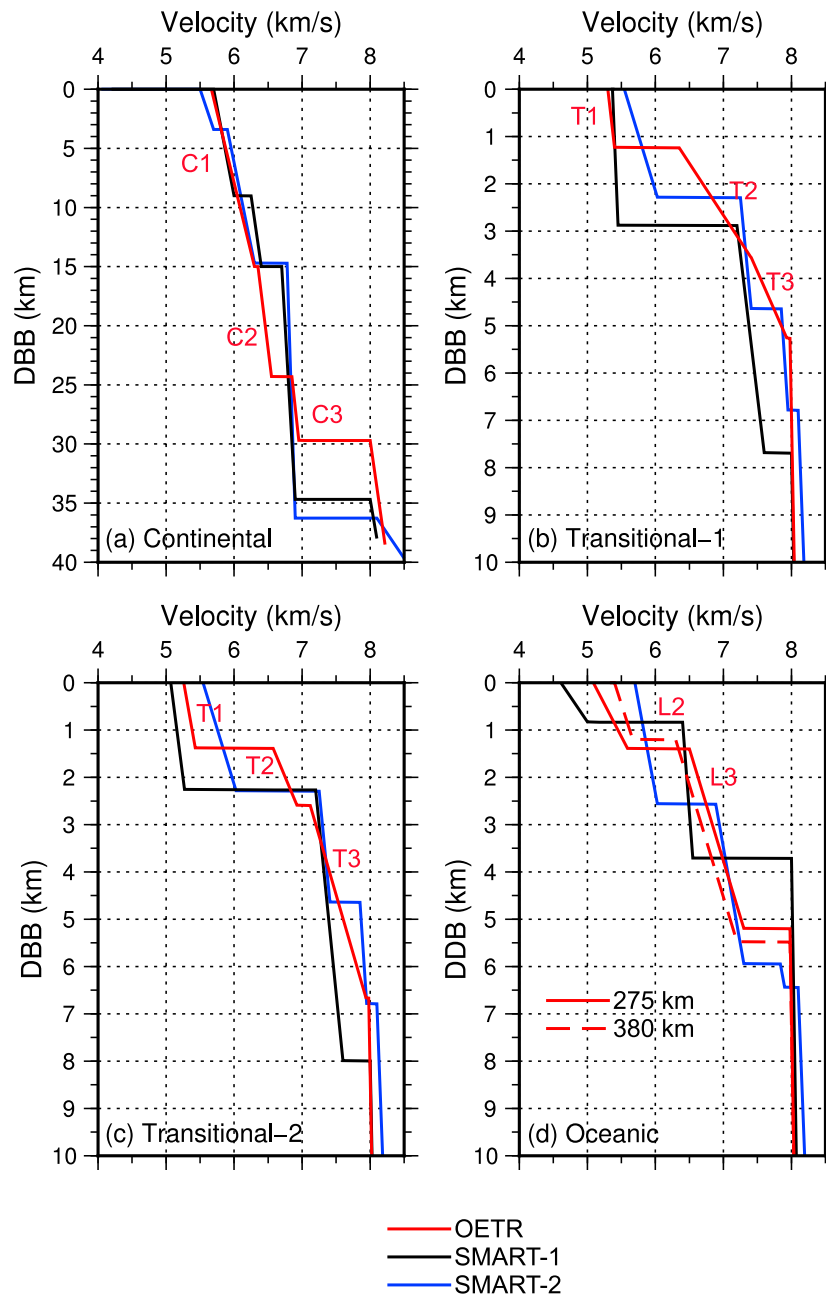
Figure 11. One-dimensional velocity versus depth functions extracted at selected locations over the three interpreted crustal zones for models OETR-2009 (red), SMART-1 (black), and SMART-2 (blue). See Figures 9a and 15 for locations on their corresponding 2-D models. Depths are shown relative to top of crystalline basement or depth below basement. Layers are labeled only for the OETR-2009 1-D velocity functions. (a) Continental. (b) Transitional-1. (c) Transitional-2. (d) Oceanic.

thickness to infinity at both the landward and seaward ends, and the bottom of the model is at 40-km depth as shown in Figure 13b. Because detailed structures are unlikely to be resolvable by gravity modeling, we combine the thin sedimentary velocity layers into two density layers. Since velocities decrease seaward, we also divide each of the two combined sedimentary layers laterally into two density blocks using a vertical boundary at the location of the greatest lateral change in velocity. In order to improve the fit with the observed gravity, the landward part of Layer S8 (distance −20 to 25 km), where the velocities are >5.2 km/s, requires a separate density model block so that a higher density can be assigned (2.56 Mg/m^3). The crustal and mantle layers are taken directly from the velocity model except for the seaward end of the oceanic Layer 3 (distance 390–420 km) where a thicker layer is required to fit the observed gravity
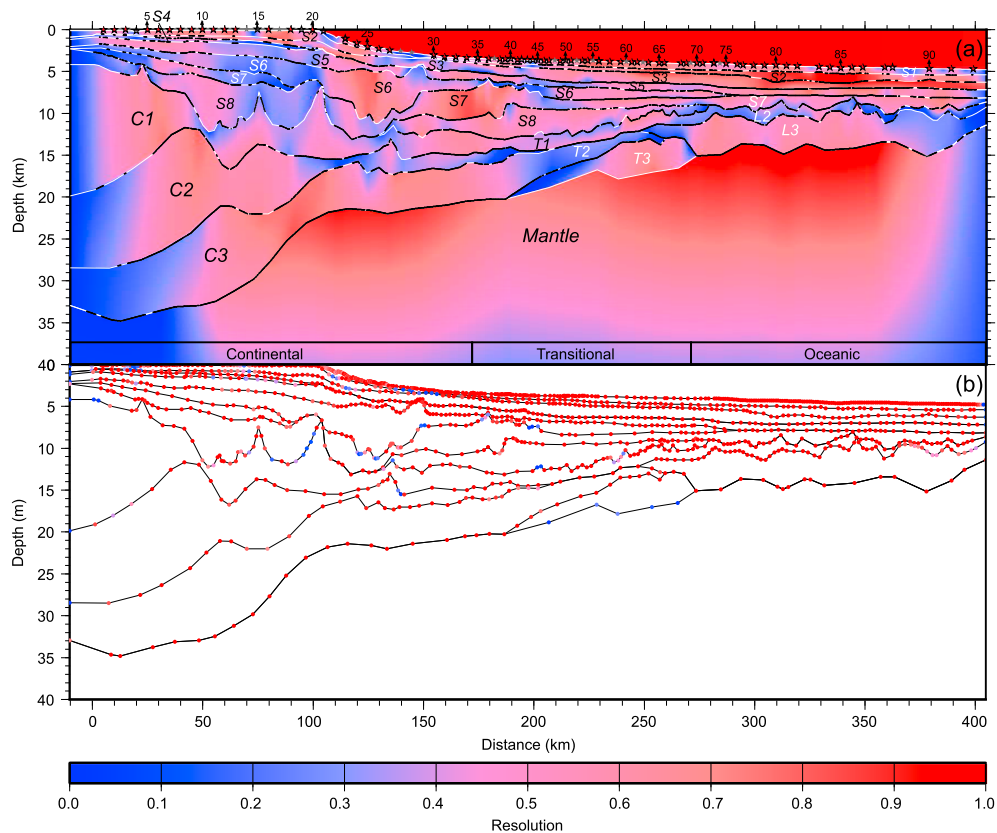
Figure 12. Model resolution plots. (a) Gridded diagonal values of the resolution matrix for all velocity nodes are shown in color, with the color scale provided at the bottom of the figure. Red means better resolved, and blue means less well resolved. Note that values for areas between layer boundaries are linearly interpolated from values along the boundaries. Black lines represent locations of layer boundaries illuminated by picked reflections, and white lines are locations without observations. See caption of Figure 9a regarding model layer names, crustal zonal interpretations, and OBS symbols. (b) Depth resolution of velocity model boundaries. Black lines are velocity model layer boundaries. Color-scaled circles are diagonal values of the resolution matrix of the depth nodes. OBS = ocean bottom seismometer.

compared with the seaward thinning layer in the velocity model. Such modification is acceptable as the seismic constraints at this part of the model are poor (Figures 9b and 12). We also separate the transitional upper crust (T1) from that of the continental zone (C1) along the 5.5-km/s contour to reflect the seaward decrease in both velocity and density (Figures 9a and 13b).

As only uniform density distribution is allowed within each block, we estimate an average velocity for each block before converting it into density. Since the upper and lower continental crust (C1 and C2) have over-lapping velocity ranges, we estimate a combined average velocity of 6 km/s and hence a density of 2.72 Mg/m^3. Small adjustments are, however, needed for the two mantle layers from the converted densities in order to fit the observed gravity. First, for the serpentinized mantle layer (T3, discussed below), the seismic velocity (7.75 km/s) converted to a density of 3.24 Mg/m^3 has to be lowered to 3.20 Mg/m^3 to explain the lack of highly observed gravity (Figure 13a). Similar adjustment was also required in Lau et al. (2006) for the serpentinized mantle layer, suggesting that the velocity-density curve used may not be sufficiently accurate for this rock type, at least in the study area. Second, we originally used a uniform normal mantle density of 3.33 Mg/m^3, which resulted in a good fit above the continental zone but produced a large-scale misfit over the transitional and the oceanic zones. Therefore, we separated the normal mantle layer into the denser continental mantle and the less dense oceanic mantle (3.283 Mg/m^3; Figure 12b) as in Funck et al. (2004) and Wu et al. (2006). Note that the abrupt boundary at ~210-km distance is arbitrary and that a diffuse transition zone would better represent the true change in the mantle properties. Note also that the density contrast across this boundary depends on the bottom depth of the model. However, our contrast of 0.027 Mg/m^3 is slightly larger (by 0.007 Mg/m^3) than those of similar mantle models in Funck et al. (2004) and Wu et al. (2006) despite having the same continental mantle density and model bottom depth. While
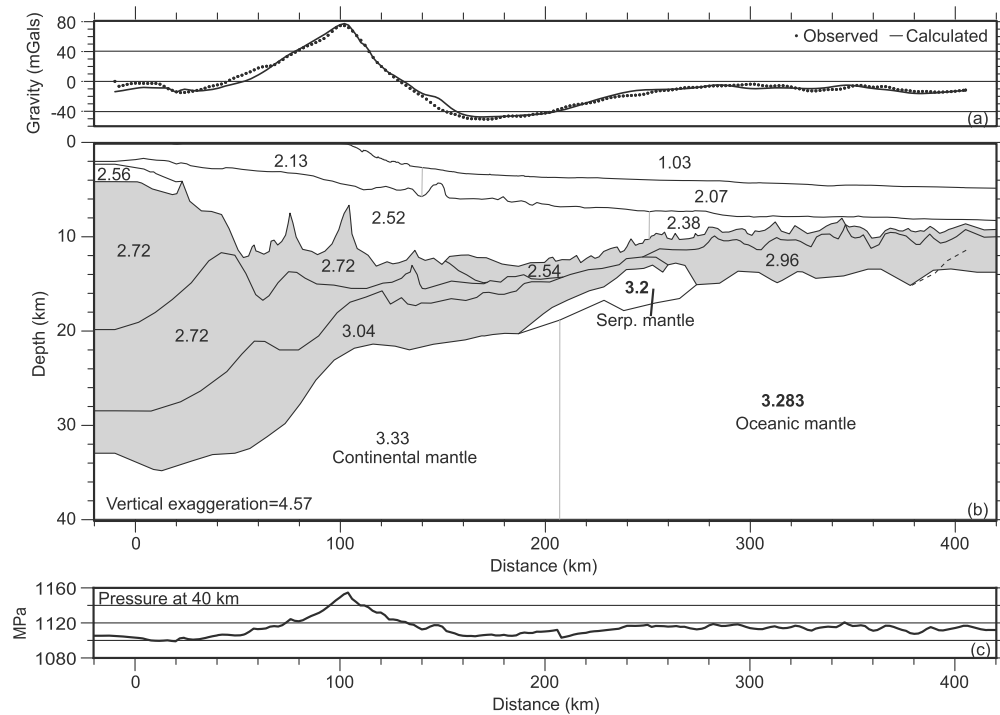
Figure 13. (b) Density model (Mg/m^3) derived from the final velocity model. The Moho depths at the seaward end of the model (for distances 390–420 km) were modified for the density model to show continuity in oceanic crustal thickness. Dashed line shows the depth as determined by velocity modeling of the seismic arrivals. The densities of the serpentinized mantle and oceanic mantle blocks, shown in bold numbers, do not follow the velocity-density conversion used for other layers in the model. (a) Observed (Sandwell et al., 2014) and calculated gravity anomalies from the 2-D density model (Figure 13b). (c) Lithostatic pressure at 40-km depth, which is the bottom of the model in (b).

the observations of a relatively lower oceanic mantle density is not uncommon (e.g., Maystrenko & Scheck-Wenderoth, 2009), the causes are yet to be understood. We also calculated the pressure based on the density model at the bottom of the model (Figure 13c). It shows that the margin is isostatically balanced at both ends, while excess pressure above and around the shelf break is supported by flexure.

5. Discussion

For joint interpretation of the wide-angle OBS velocity model and the coincident GXT-2000 MCS reflection image, we first convert the GXT-2000 prestack depth-migrated section (Play Fairway Analysis Atlas, 2011) to TWTT using the corresponding migration velocity. The resulting time section is then converted back to depth by vertical stretching using the final wide-angle OBS velocity model produced in this work (Figures 9a and 14). The velocity model and the reflection image are displayed superimposed in Figures 14 and A1, allowing for a unified interpretation. The good correspondence between the two results is not surprising considering that the MCS reflection image was an important constraint used for the construction of the velocity model boundaries. Hence, a combined analysis using the depth-converted MCS section (Figure 14), the final velocity model (Figures 9a and 14), and the downhole seismic and stratigraphic interpretations of wells P-52 and D-76 (Figure 10) forms the basis of the zonal interpretation (Figure 9a) presented in the first three subsections of section 5: continental zone (−10 to 172 km), transitional zone (172–272 km), and oceanic zone (272–405 km), all of which include a comparative analysis with relevant nearby profiles across the Nova Scotia margin. The final subsection of section 5 consists of a comparison with existing results from the MIRROR-1 conjugate profile on the Moroccan margin.

5.1. Continental Zone

Stratigraphic interpretation of postrift sedimentary layers along the coincident OETR-2009 velocity and GXT-2000 reflection profiles is relatively straightforward as horizon depths are calibrated by boreholes within the Huron Subbasin beneath the shelf (Figures 10 and 14). According to these profiles, both the thinner
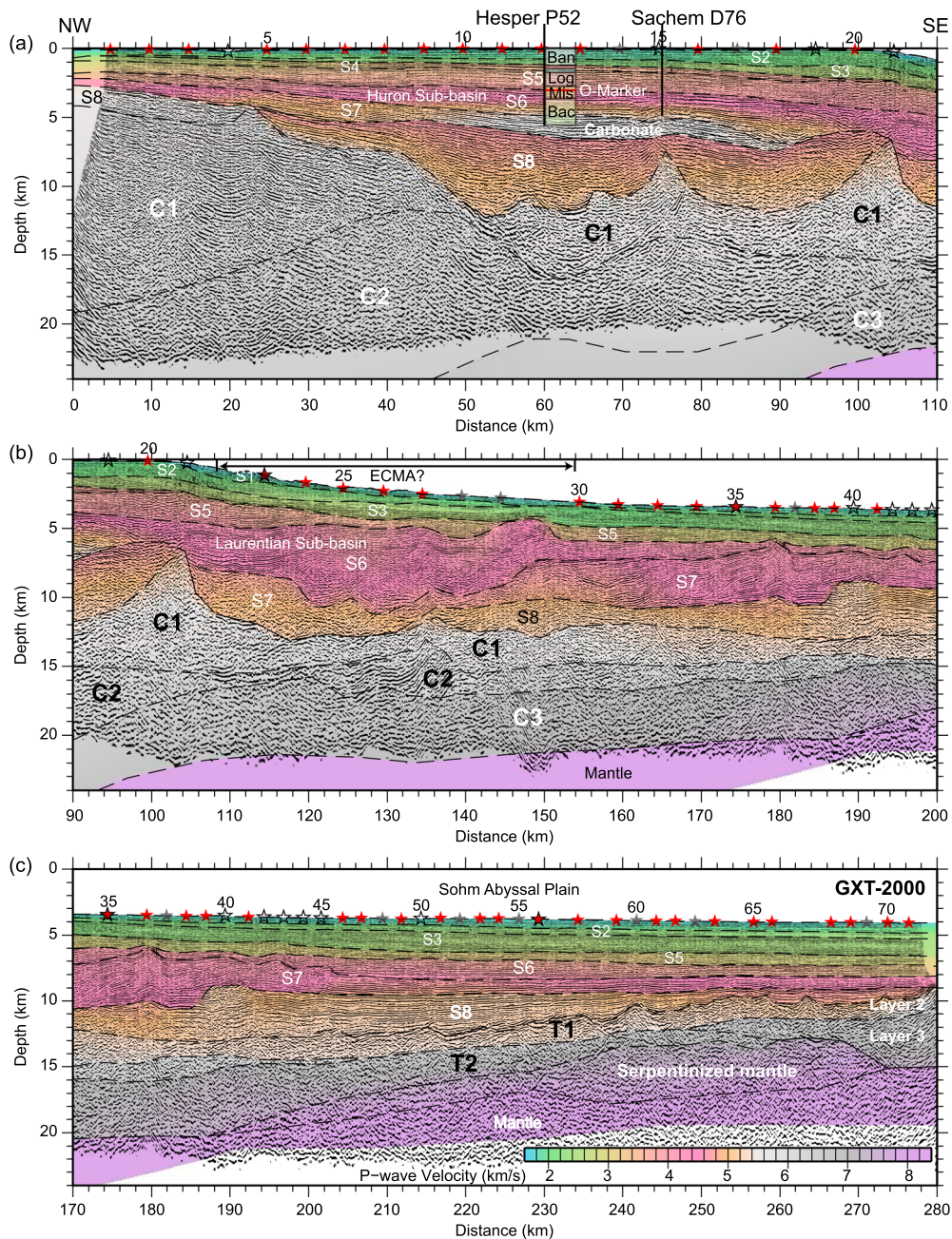
Figure 14. MCS profile GXT-2000 (foreground reflectivity) after conversion to depth using the OETR-2009 final velocity model (color background). Dashed lines are model boundaries; stars are OBS positions. See Figure 9 for explanation to labeling of layers and OBS fill colors. Black vertical lines are project borehole locations. Stratigraphic formations are taken from Figure 10. The original continuous profile is divided into three detailed subplots to emphasize different regions of interest: (a) moderately thinned continental crust beneath the shelf; (b) highly thinned continental crust beneath the slope and rise; (c) continent-ocean transition. See Figure 9 caption for ECMA. MCS = multichannel seismic; OBS = ocean bottom seismometer; ECMA = East Coast Magnetic Anomaly.

(~0.5 km) Layer S4 and the thicker (<2 km) Layer S7 carbonate banks, which are potential petroleum reservoirs, are limited to the shelf (Figure 14a). Note that the actual top of the Late Jurassic carbonate bank may be at the Baccaro top boundary within Layer S6 (MacLean & Wade, 1993; Wade & Maclean, 1990; Wade et al., 1995). The Layer S7 carbonate bank reaches unusually high velocities (5.8 km/s) and is here referred to as a HVL. With only three OBSs (15–17) directly above the carbonate bank, Funck et al. (2004) were unable to resolve its basal depths and hence extended it down to the basement for simplicity. However, we are able to constrain with high depth resolution (Figure 12b) the base boundary of this layer

using constrains from at least seven OBSs directly above the carbonate bank and the observed reflections from the GXT-2000 reflection image (Figure 14a). We find that the sub-HVL unit creates a velocity inversion (see section 3), as would be expected from strata composed of clastic sediments.

A larger number of OBSs do not, however, solve the problem of the lack of turning rays through the sub-HVL unit so the velocities of these deep clastic sediments remain poorly constrained. Boreholes also do not penetrate deep enough to constrain velocities in this layer (Figure 14a). Nevertheless, we propose a velocity inversion for this section of the OETR-2009 model with interpolated sub-HVL sedimentary velocities, as described in section 3, to explain the observed step backs in the OBS gathers. Because the greater uncertainty in the velocity of the sub-HVL sedimentary unit translates into larger uncertainty in the depths of basement and deeper boundaries such as Moho for this area, we ran sensitivity tests to constrain them. This was accomplished by producing 10 initial models, each assuming a uniform velocity between 4.5 and 5.4 km/s for the sub-HVL unit with a step of 0.1 km/s and running inversions to minimize the misfit. The resulting best fit models suggest that the uncertainty in Moho depths is only <1 km (c.f. <2.5 km in Funck et al., 2004).

Another major difference between the SMART-1 (Funck et al., 2004) and this OETR-2009 model is the absence of salt diapirs beneath the shelf in our model (Figure 9a). Instead, basement highs (see top of C1) are interpreted, according to their velocities, as large-scaled (~15-km wide and ~5-km high) tilted basement blocks. This also agrees with observed tilted sediments within the basin (S8) that mostly dip landward (Figure 14a), a common feature of the synrift infill (Prosser, 1993; Wu et al., 2006). The Huron Subbasin is, hence, interpreted as a series of smaller half-grabens rather than a large slope basin as suggested in the SMART-1 model. The basement model of OETR-2009 also fits the observed gravity (average misfit ~4 mGal; Figure 13a) much better than the SMART-1 model, which shows a 3 times greater average misfit (~12 mGal) over the equivalent structures. Alternatively, dipping sediments can also be due to salt being squeezed out of the basin by the overburden (Albertz & Beaumont, 2010) although the continental block, as proposed seaward, would have blocked such migration. Note that salt structures are, however, imaged along the profile within the Laurentian Subbasin and seaward in both diapiric and canopy forms (Figures 4, 14b, and 14c) but were merged in our OETR-2009 velocity model into the surrounding sediment as one layer. The velocity contrasts across the salt boundaries are, therefore, smoothed out, causing minor distortions to the definition of their structural shapes.

Figure 11a compares the velocities of the thickest three-layered continental crust of the OETR-2009, SMART-1 (Funck et al., 2004), and SMART-2 (Wu et al., 2006) models. The total thickness of the OETR-2009 crust is ~4 km thinner than beneath SMART-1, which is also ~2 km thinner than beneath SMART-2, suggesting that the full-thickness crust thins slightly to the northeast. This is in contrast to a review by Klingelhoefer et al. (2016), where unthinned crust is found to be thicker northward on the African counterpart, but the crust there may have been affected by the postopening collision between the Africa and Iberia plates. Alternatively, the thickest continental crust modeled along the OETR-2009 profile, being farther seaward than in the SMART-1 and SMART-2 models (Figure 1), may have already been slightly thinned, with the unrifted crust (likely ~34-km thick based on the SMART models; Figure 11a) located farther landward of the profile. In addition to a much thinner lower crust (C3), the middle crust (C2) velocities of 6.4–6.6 km/s also deviate from the velocities modeled along SMART-1 and SMART-2 (~6.8 km/s) for the same depths (15–26 km, Figure 11a), suggesting different rock material in place of the upper part of the SMART-1 and SMART-2 lower crust. Since such a large-scale structure is unlikely to have completely pinched out less than 100 km southwest toward SMART-1, we interpret that the OETR-2009 middle crustal velocity is a refinement to the upper part of the lower crust in the SMART-1 and SMART-2 models (Figure 11a). Despite this, the middle crust is more continuous in velocity with the upper crust than with the lower crust, which is a feature shared with SMART-1 and SMART-2 models. Therefore, even if the same density is used for modeling of both the upper and middle crust, a very good fit between the calculated and the observed gravity will still be achieved (Figure 13).

Beaumont (2010) proposed that early pinching out of the middle crust could be an indication that it is strong relative to the other crustal layers, which can eventually lead to a narrow margin at the breakup. Wide-angle (Figures 12a and 5) and near-incidence (Figure 14a) reflections in the OETR-2009 data that arise at the transition from the upper to the middle crust support a well-defined crustal boundary, despite only a moderate jump in the modeled velocities. The presence of middle crust farther seaward along the OETR-2009 profile

than modeled along the SMART-1 profile (Funck et al., 2004), therefore, does not support a strong middle crust beneath NE Nova Scotia and may explain the observed widening of the Scotian margin from southwest to northeast.

If variations in thinning between the modeled crustal layers, regardless of the underlying mechanism, are considered to represent depth-dependent thinning, then the observed offsets in the necking zones of the three OETR-2009 crustal layers clearly indicate depth-dependent thinning of the continental crust (Figure 9a). One such example is the area around a basin bounding normal fault beneath the landward side of the Huron Basin (42- to 92-km distances; Figure 14a), where the three crustal layers may still be well coupled within each fault block, but the depth-dependent thinning is nevertheless caused by the fault slip. In the two-layered weak crustal models of Beaumont (2010), depth-dependent thinning commonly occurs because the lower crust, being hotter, flows more efficiently than the upper crust. Such flow would result in an ultrawide (>200 km) margin (Huismans & Beaumont, 2011) that is wider than in our model and a Moho that is smoother than we observe. Similar models involving an intermediate strength lower crust that flows at fault block scales have also been proposed (Pérez-Gussinyé et al., 2003) for the Galician Inner Basin. The OETR-2009 Moho seems to more resemble these models with intermediate strength lower crust, where crustal thinning is produced by sequential oceanward faulting (Brune et al., 2014; Ranero & Pérez-Gussinyé, 2010; Ros et al., 2017) with fault block scale (30–50 km) lower crustal flow. Also, the Moho is less smooth than in the ultrawide margin model of Huismans and Beaumont (2011) but not as angular as would be produced by through-cutting crustal faults.

Another interesting feature common to all numerical models of Beaumont (2010) is the lack of a classic, monotonically seaward thinning crust and rising Moho (e.g., Funck et al., 2004; Wu et al., 2006). Instead, the crust can at places thicken seaward, with the Moho dropping downward in the seaward direction in relation to a downward motion along a normal fault in the upper crust, before rising again toward breakup, thus forming a crustal swell at the distal margin. Such boudinaging of crust is well documented in a recent well-constrained OBWAVE velocity model of an abandoned rift in the Orphan Basin where a ~600-km-wide zone of attenuated crust was formed (Lau et al., 2015). We also observe in OETR-2009 model a similar Moho dip down (115–134 km) and the associated minor distal crustal swell (117–190 km). In both models, the velocity of the lower crust of the distal crustal swell increases slightly from their landward counterparts (Figure 9a). Furthermore, the prerift lower crust may also be of higher velocity toward Morocco as will be discussed later in section 5.4.

5.2. Transitional Zone

Magma-poor transitional zone is interpreted at model distances 172–272 km based on the Layers T1–T3 velocity structures modeled (Figures 9a and 15a), which are not typical of continental or oceanic crust. Two subzones can be distinguished from variations in the velocity of Layers T1 and T2 (Figures 11b, 11c, and 15a) that parallel similar changes in SMART-1 (Figures 11b, 11c, and 15b). A more laterally uniform transitional zone is, however, modeled for SMART-2 (Figure 15c).

For the OETR-2009 profile, the velocity of Layer T1 is modeled as intermediate between that of the continental upper crust (C1) landward and the oceanic Layer 2 (L2) seaward (Figure 9a). Modeling any complexities within this layer with confidence is not possible due to its poor sampling (Figures 9b and 12a). In other words, there are too few observations to support a more complex model of Layer T1. Fortunately, the basement top reflection (Figure 14) also demonstrates a transition between a smoother unreflective continental basement landward (<172 km) and a highly rugged and reflective oceanic basement seaward (>272 km). Furthermore, the normal continental upper crustal velocity of 5.5–6.3 km/s is completely missing within this zone. Our interpretation of Layer T1 is, therefore, that of a highly thinned (<2-km thick) continental crustal layer characterized by gradual seaward increase in basaltic melt emplaced within it until embryonic oceanic crust takes over at the seaward limit of the transitional zone (Figure 15a). This is in contrast with a discrete, continent-ocean boundary style transition from continental into oceanic Layer 2 modeled for SMART-2 (Figures 11b, 11c, and 15c) and more similar to the two-stage transition in the upper crust of the SMART-1 model (Figure 15b). However, one-to-one comparison of the OETR-2009 model with SMART-1 and SMART-2 models is challenging due to the poor resolution of the sparse OBS recordings on SMART profiles.
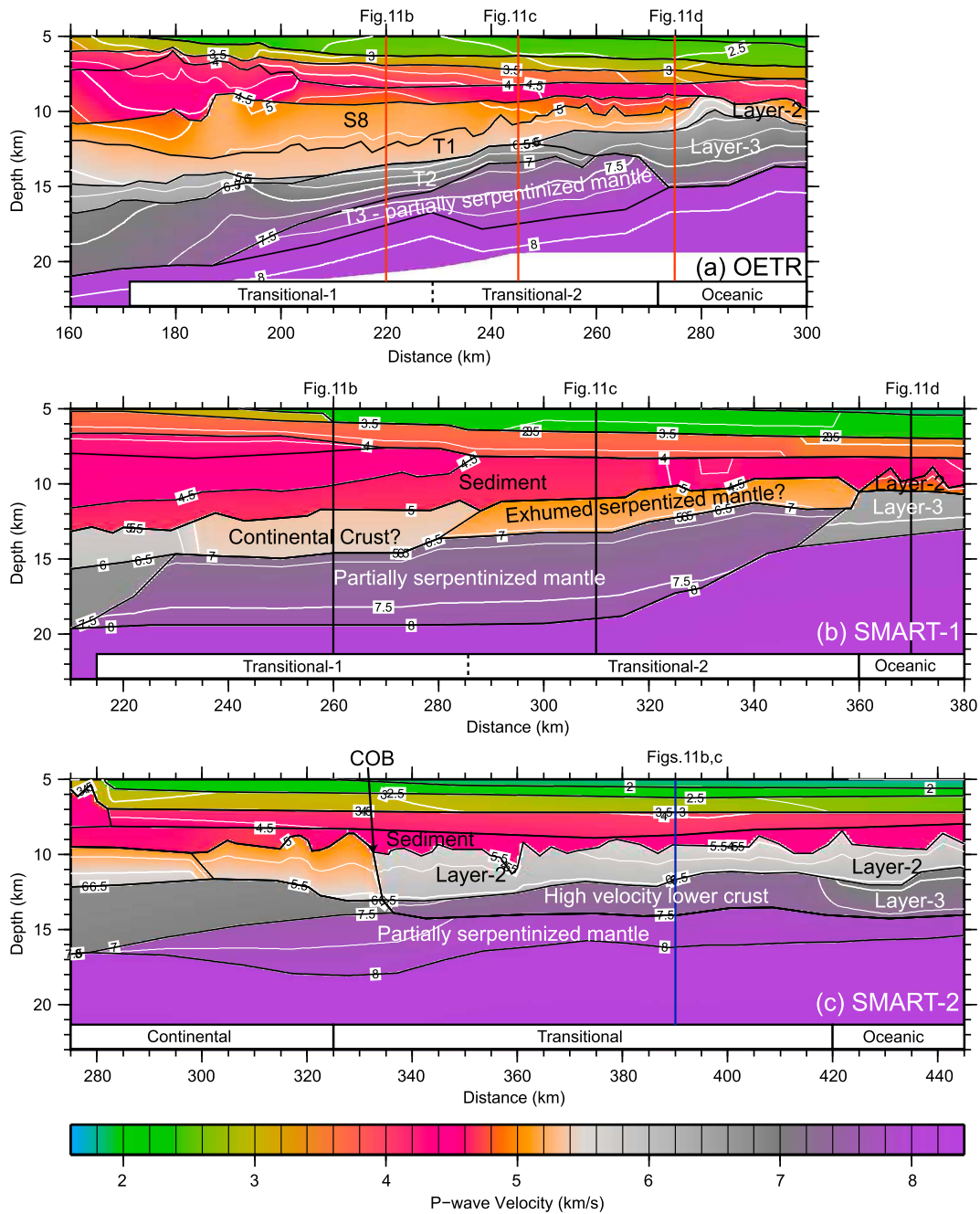
Figure 15. Along-strike comparison of the COT across the northeastern Nova Scotia margin based on RAYINVR *P* wave velocity models of profiles (a) OETR-2009 (Figure 9a), (b) SMART-1 (Funck et al., 2004), and (c) SMART-2 (Wu et al., 2006). See Figure 1 for locations of profiles. Red, black, and blue vertical lines show locations of 1-D profiles plotted in Figure 11 as labeled at the top. Velocities are contoured every 250 m/s. COT = continent-ocean transition.

The base of Layer T1 does not coincide with any high-amplitude reflection event in the GXT-2000 section despite a large velocity contrast modeled across the boundary (Figure 14c) and observed wide-angle reflection (Figure 12a). The T1-T2 boundary is, therefore, one that allows very low reflected amplitude at near off-sets. The high gradient lower transitional crust (T2) of the OETR-2009 model can be interpreted as a buffer zone for the large velocity increase between the base of Layer T1 and the top of Layer T3. It is difficult to deduce a meaningful geologic interpretation for this layer. The presence of Layer T2 facilitates a very good χ^2 value (1.26) for the fits of the layer below, that is, T3 (P_{n1}; Table 2). The highly resolved velocities of 7.1–7.9 km/s for the thicker section of Layer T3 (transition 2) provide a robust evidence for the presence of

partially serpentinized mantle, with the degree of serpentinization decreasing smoothly downward toward the normal mantle. This interpretation is extended into the thinner section landward where the resolution is much lower since there are no major differences in reflectivity and velocity structures between the two sub-zones. Based on this interpretation, the landward end of contour 7.1 km/s defines the landward end of the transitional zone (172-km distance; Figure 9a), which also coincides with the seaward end of contour 5.5 km/s of the upper continental crust (C1) near where Layer C2 pinches out.

There are two scenarios to explain the seaward thickening of Layer T3 as Layer T2 thins and therefore the formation of the two subtransitional zones. In the first scenario, the seaward increase of the dominance of accretionary processes within the upper crust (T1) lowers the extent of brittle faulting, restricting high degrees of serpentinization (T2) to only shallow depths, resulting in a thinner moderately serpentinized (50–70%; T2; Watanabe et al., 2007) and thicker mildly serpentinized mantle (<50%; T3) layers. Alternatively, T1 and T2 are upper and lower continental or oceanic crust that is thinner seaward, promoting more brittle deformation and allowing more water to serpentinize a thicker layer of mantle seaward. This mantle layer has, however, cooled quickly enough to prevent massive decompressional melting that would form either igneous underplating or normal oceanic crust. The lack of melting in the extreme case can lead to mantle exhumation as proposed for zone transitional 2 along the SMART-1 model (Figure 15b).

Based on the detailed discussion of continental stretching presented in section 5.1 and the presence of very thin crust within the COT, we challenge the interpretation of an underplated magmatic body for the OETR-2009 model produced by GeoPro GmbH (Play Fairway Analysis Atlas, 2011), which was suggested to be either beneath thinned continental crust or part of the transitional crust (Luheshi et al., 2012). First, any voluminous volcanic intrusion within or beneath the crust would result in further thickening of the minor distal crustal swell (117–190 km) instead of the modest seaward thickening modeled. Second, a velocity of ~7 km/s within the lower crust of the distal crustal swell may be too low for a pure gabbroic underplate even though the low-velocity gradient can be compatible with it. Third, we do not observe any SDRs in the GXT-2000 reflection section (Figure 14b), which suggests a lack of wide-spread magma flow and so only limited underplating is expected. Lastly, it is difficult to explain the shutting off of a synrift magma source responsible for the underplate, when followed by a substantial episode of mantle serpentinization as a result of delayed seafloor spreading due to lack of melt. The differences between the Luheshi et al. (2012) and our velocity model of the OETR-2009 data, which lead to different interpretations, are not possible to explain because, unfortunately, the Luheshi et al. (2012) publication only presents the produced layered velocity model result and does not provide any of the material necessary to support it.

The results of magnetic modeling of a much weaker ECMA toward the northeastern Nova Scotian margin (Figure 1) also suggest a lack of underplate for this region (Dehler, 2012). The magnetic sources for SMART-2 and SMART-1 were modeled as only a thin (<2- and ~1-km thick, respectively) volcanic layer at the seaward end of the continental zone. It is important to note that these volcanic layers were not resolvable by wide-angle seismic data (Funck et al., 2004; Wu et al., 2006) but were nevertheless added to the wide-angle crustal models in order to match the observed magnetic anomalies. This is unlike the SMART-3 profile farther southwest, where SDRs are observed and a much thicker (~4 km) volcanic layer is modeled with seismic data (Play Fairway Analysis Atlas, 2011).

5.3. Oceanic Zone

Our oceanic crust modeled seaward of the transition zone shows a single Layer 2 at the top and a thicker Layer 3 below, both with velocity structures that are consistent with those of recent well-constrained crustal models (Newman et al., 2011) and an earlier compilation of oceanic crustal velocities (e.g., White et al., 1992). Because ocean crust in this zone is thicker than the embryonic oceanic crust landward, mantle serpentinization was limited by both fewer interconnected crustal-scale faults that permit water penetration and higher mantle temperature at the base of the crust (Bayrakci et al., 2016; Pérez-Gussinyé & Reston, 2001), causing the serpentinized mantle layer to pinch out seaward.

Despite being thicker than the embryonic oceanic crust found at the seaward end of the transitional zone (model distance of ~250–275 km), the modeled full thickness of the early oceanic crust of 3.5–6 km (model distance ~275–400 km) is less than the thickness of normal oceanic crust of 6–7 km (Aghaei et al., 2014; White et al., 1992). Because both modeled oceanic crustal layers (2 and 3) are well constrained by the

dense high-quality OBS data, especially Layer 3 (Figure 12), and the thickness of both layers varies (Figure 9a), it is likely that both of these layers are thinner than those found in normal oceanic crust but to a varying degree. However, the presence of a well-developed Layer 3 is sufficient to rule out ultrathin oceanic crust, as its Layer 3 is often fully or partially missing (Davy et al., 2016; Funck et al., 2003).

The thinner than normal oceanic crust in the study area is not surprising considering that the spreading rate during the early stages of drifting in the central North Atlantic, though still debated (Bird et al., 2007; Klitgord & Schouten, 1986; Labails et al., 2010; Louden et al., 1987; Schettino & Turco, 2009), seems to have varied from ultraslow to slow (16–22 mm/year). At these spreading rates the melt supply is thought to be low due to the relatively low mantle temperature resulting from its slow ascent. Further supporting this interpretation, the modeled velocity and thickness of Layer 2 is particularly variable (Figure 9a), in agreement with the episodic nature of melt extrusion and intrusion and crustal extension commonly observed at slow to ultraslow spreading ridges (Dick et al., 2003; Louden et al., 1996). However, this variation may be a result of inconsistency in the interpretation of wide-angle basement reflection across different OBSs. Without coincident MCS control at the seaward end of the OETR-2009 profile, deep sedimentary phases can potentially be misinterpreted as being crustal.

According to the 1-D velocity-depth profiles from this zone, the OETR model sits between the low bound SMART-1 and the high bound SMART-2 models in terms of both velocity and thickness of Layer 2 (Figure 11d). Therefore, despite the difficulty in modeling Layer 2, its modeled velocities are consistent with those of the other models in the area. The OETR-2009 model also has a Layer 3 with a relatively high velocity gradient and velocities that fall within the SMART-1 and SMART-2 model bounds (Figure 11d). However, the low gradient, low-velocity Layer 3 (6.5 km/s), and a total crustal thickness of ~4 km of the SMART-1 model are not typical for normal oceanic crust.

5.4. Conjugate Comparison

Conjugate studies are essential for the full understanding of the development of a rift system. First near-conjugate Nova Scotia and Morocco margin comparisons were based on SISMAR-4 profile (Contrucci et al., 2004) on the Moroccan margin and SMART-1 (Funck et al., 2004) on the northeastern NS margin (Maillard et al., 2006; Tari & Molnar, 2005). The margin structures in these two profiles show a high degree of asymmetry (Reston, 2009), but it is not possible to rule out along-strike variations in margin structure. More recent conjugate comparisons were presented using the SMART-1 profile on the Nova Scotia margin and the MIRROR-1 profile on the Morocco margin (Biari et al., 2017; Klingelhoefer et al., 2016), which, according to a plate reconstruction using the poles of either Seton et al. (2012) or Sahabi et al. (2004), is the direct conjugate margin. However, the resolving power of the SMART-1 data with instrument spacing of 20–40 km is much lower than for the MIRROR-1 profile with instrument spacing of ~10 km. In Figure 10, we show a juxtaposition of our detailed OETR-2009 final model, found only ~100 km northeast from the SMART-1 profile and that of the MIRROR-1 wide-angle seismic profile (Biari et al., 2015). Since no magnetic anomalies (e.g., M-series) can be identified near the seaward end of the conjugate models as a reference for reconstruction, the two models are simply juxtaposed at their seaward ends with the unconstrained extremes removed (i.e., profile ends where crossing rays are absent).

Large-scale asymmetry can be seen from Figure 16. First, the MIRROR-1 model (Biari et al., 2015) suggests a three-layered unthinned continental crust that is thicker eastward (max thickness is 36 km). The crustal velocities of each individual sublayer are also slightly higher (0.25 km/s) than those of the OETR-2009 model. While depth-dependent thinning exists on both models, the MIRROR-1's crust thinned more uniformly to produce smoother crustal boundaries, forming a rough-smooth asymmetry across the conjugates. However, this difference in the morphology of the crust can also be a result of the greater resolving power along the OETR-2009 profile due to smaller OBS spacing and different modeling strategies. While the proposed possible continuation of the ECMA is identified at the seaward end of thinned continental zone on the OETR-2009 model (Sibuet et al., 2012) as a very low magnitude magnetic anomaly, the S1 (or West African Coast Magnetic Anomaly) is interpreted at the landward end of zone Oceanic-1 on the MIRROR-1 model, resulting in a wide-narrow asymmetry in the width of thinned continental crust across the conjugates. Such asymmetry may be caused by the difference in the thicknesses of synrift sediment (velocity > 4.5 km/s) on the two conjugate margins, which is supported by results from numerical modeling (Beaumont, 2010). This may compound with other possible mechanisms for asymmetry such as sequential faulting (Ranero &
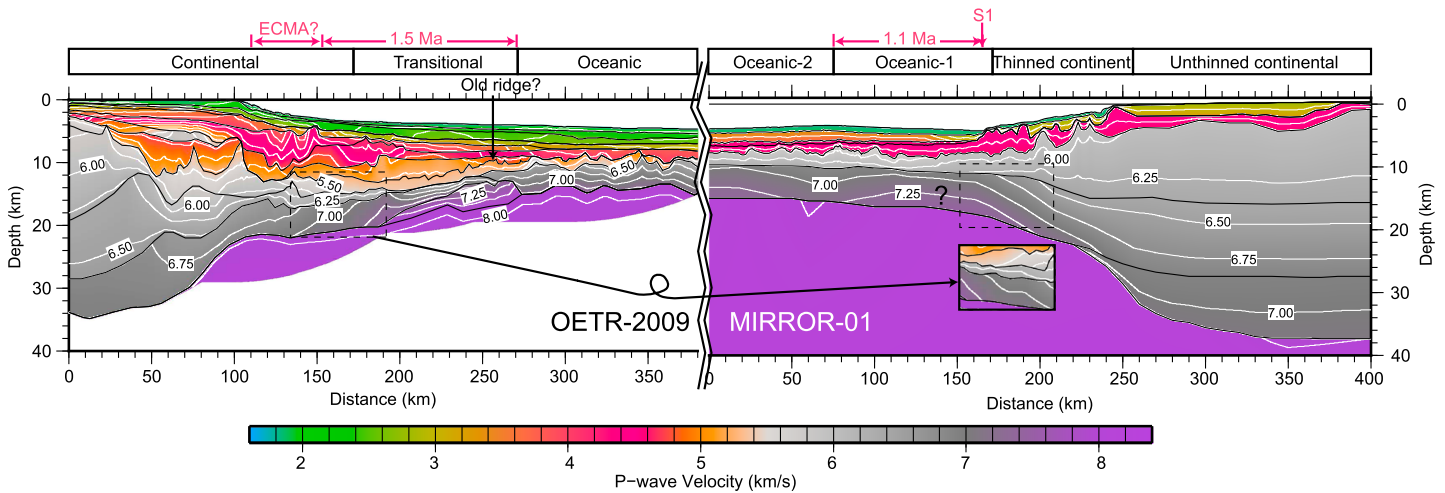
Figure 16. Conjugate comparison of RAYINVR *P* wave velocity models between Profile OETR-2009 (Figure 9a) on the Nova Scotia margin and Profile MIRROR-1 on the Moroccan margin (Biari et al., 2015). Crustal zones for the Moroccan margin are taken from Biari et al. (2015). Question mark represents interpretation discussed in text. Velocities are contoured every 250 m/s. Dashed line rectangles on MIRROR-1 and OETR-2009 profiles show corresponding areas at the conjugate margins. The velocities within the OETR-2009 rectangle are also shown on the right panel for comparison. ECMA and S1 are magnetic anomalies. See text for horizontal age distances in million years (Ma). ECMA = East Coast Magnetic Anomaly.

Pérez-Gussinyé, 2010) with rift migration (Brune et al., 2014, 2017), strength softening in the dominant rheology that controls the extension style (Huismans & Beaumont, 2003), and lateral heterogeneities (Wenker & Beaumont, 2016). Note also that the magnitude of subsidence is also much greater for the OETR-2009 model. Furthermore, a long-wavelength deepwater bulge that affects the seafloor to basement structures exists only on the MIRROR-1 model and may be related to the impingement of plume material from the Canary Plume to the south (Benabdellouahed et al., 2017).

By assuming an average full crustal thickness of 34 km on the Canadian side and 36 km on the African side, the seaward limit of reconstructed unextended continental crust would be at 85-km model distance (60-m isobaths) and 222-km model distance (1.6-km isobaths), respectively. This allows for an update on plate kinematic reconstruction to prerifting times. The continental extension (from reconstructed unextended crust to continental breakup) is also wider for the OETR-2009 model (85 km) than for the MIRROR-1 model (52 km), implying that more of the stretched continental crust was left on the Canadian side (ratio ~ 3:2). Despite the above asymmetries, the velocity structures of the seaward end of the lower crust into the transitional crust of the OETR-2009 model and that of the middle crust underneath Anomaly S1 of the MIRROR-1 model are very similar (insets; Figure 16). This may suggest a more symmetrical thinning before lithospheric breakup.

Farther seaward, we regard the landward oceanic zone (Oceanic-1) of the MIRROR-1 model (Biari et al., 2015) as a transitional zone similar to the COT in the OETR-2009 model because: (1) it shows a gradual change in velocity between the surrounding zones (Figure 16) and (2) an anomalous body of velocities either too high for normal oceanic crust or too low for normal mantle is present only within these two zones. Therefore, we regard these zones to be equivalent and contemporary where atypical oceanic crust is interpreted for both. Consequently, zone Oceanic-1, appearing possibly equivalent to the transitional zone of the OETR model, may also consist of a thin embryonic oceanic crust above a serpentinized mantle layer. We propose that while the Oceanic-1 upper crust may be embryonic oceanic crust, the lower crust may be space originally occupied by serpentinized mantle and later intruded by volcanic melt from the Canary hotspot (Holik et al., 1991). This also agrees with the highly reflective and smooth Moho and the larger crustal thickness on the Moroccan margin compared with its Canadian conjugate. The emplacement of melt would have overprinted the originally shallower but rougher Moho. Therefore, the asymmetry observed across the conjugates may alternatively be the result of the postrift volcanic activity that affected only the African margin.

The hotspot episode did not, however, affect the width of the margins. Using the distance between the proposed ECMA continuation and the oceanic crust of the OETR-2009 model and a half-rate of 0.8 cm/year

(Labails et al., 2010), the first normal oceanic crust was formed 1.5 Ma after ECMA assuming no ridge jump (Figure 16). The same calculation yields 1.1 Ma for zone Oceanic-1 in the MIRROR-1 model and so only a minor eastward ridge jump of 16 km from the old ridge (equivalent to 0.2 Ma) is required to account for the observed asymmetry. This is contrary to Sibuet et al. (2012) who proposed a dramatic ridge jump all the way to Anomaly S1 which was regarded as contemporary to the landward limit of our oceanic zone on the Canadian side.

Similar to our interpretation, a dramatic ridge jump is not required in the Biari et al. (2017) interpretation, which is based on the comparison between their MIRROR-1 model and SMART-1 model of Funck et al. (2004). Biari et al. (2017) proposed a core complex mode of seafloor spreading to account for magmatic accretion of Zone Oceanic-1 on the Moroccan side and formation of contemporary amagmatic COT by mantle exhumation on the Canadian side. However, while the high velocities within the deeper section of the thicker proto-oceanic crustal (or embryonic crustal) Layer 3 in zone Oceanic-1 on the Morocco side may result from inclusion of serpentinite during accretion (Biari et al., 2015), exhumed mantle is not observed in the OETR-2009 data and so our results do not support a core complex model. Nevertheless, we note that the MIRROR-1 and OETR-2009 profiles are laterally offset by ~100 km and that any major short wavelength along-strike variations in margin structure would impact our interpretation. Most useful additional constraints needed for this conjugate comparison would best be obtained by collecting margin-parallel wide-angle OBS profiles on both sides.

6. Conclusions

The presented OETR-2009 layered *P* wave velocity model is well constrained by, and optimally fitted within uncertainties to, observations from wide-angle seismic data. It provides the most detailed velocity model of the northeastern Nova Scotia rifted continental margin from the continental, across the transitional, to the oceanic crustal zones. The newly developed OETR-2009 model shows a high level of consistency with the coincident GXT-2000 MCS profile, gravity data, and nearby borehole information. Considering all available information, including a comparison with the SMART velocity models on the Nova Scotia margin and the MIRROR-1 model on the conjugate Moroccan margin, we disagree with the recent proposition that the entire Nova Scotia margin segment is magma rich (Luheshi et al., 2012) and instead support the previously established magmatic-to-amagmatic transition between Profiles SMART-2 in the central Nova Scotia margin and SMART-3 in the southwest (e.g., Wu et al., 2006). Our interpretation of an amagmatic northeastern Nova Scotia margin is based on the key features of the OETR-2009 model.

1. A large sediment thickness (up to 12-km thick) is modeled (velocities = 1.7–5.8 km) along the profile. The youngest (Paleogene) sedimentary package has velocities (1.7–2.9 km/s) significantly lower than that of the older Wyandot formation or equivalent. For the older package (Triassic-Cretaceous) within the Huron Basin (shelf), the O-Marker represents only a minor velocity contrast beneath which the velocity increases steeply to that of a Jurassic carbonate bank (HVL) with fairly uniform velocity (~5.8 km/s) up to 2-km thick. Underneath, a velocity inversion produces a "shadow layer" interpreted as synrift to early postrift clastic sediment infilling two half-grabens.

2. Full thickness (30 km) continental crust at the inner shelf is comprised of upper (5.6–6.3 km/s), middle (6.4–6.6 km/s), and lower (6.9–7.0 km/s) crustal layers based on their decrease in velocity gradient downward. The middle crust is not a rheologically strong layer as it extends as far seaward as the upper and lower crust.

3. The upper crust started thinning first (farthest landward), forming the shallow Huron Basin beneath the outer shelf. Thinning of middle and lower crust starts farther seaward beneath the central Huron Basin, where two large tilted upper crustal blocks and a possible listric fault, which coincides with top middle crust, are observed. Seaward of the shelf break, the crust first thickens and then thins mainly within the lower crust, forming a minor crustal swell at the distal margin until the seaward end of the continental zone (~70 km from the shelf break).

4. A deepwater (depth > 3.5 km), 100-km-wide transitional zone between the continental and oceanic zones is characterized by a low velocity (5.3–5.4 km/s), low gradient, very thin (<2-km thick) upper crust above a high velocity (6.3–7.5 km/s) and high gradient lower crust that thins seaward from 4.7-km thick to pinch out. The upper crust was formed by a gradual seaward increase of basaltic melt emplaced between small-
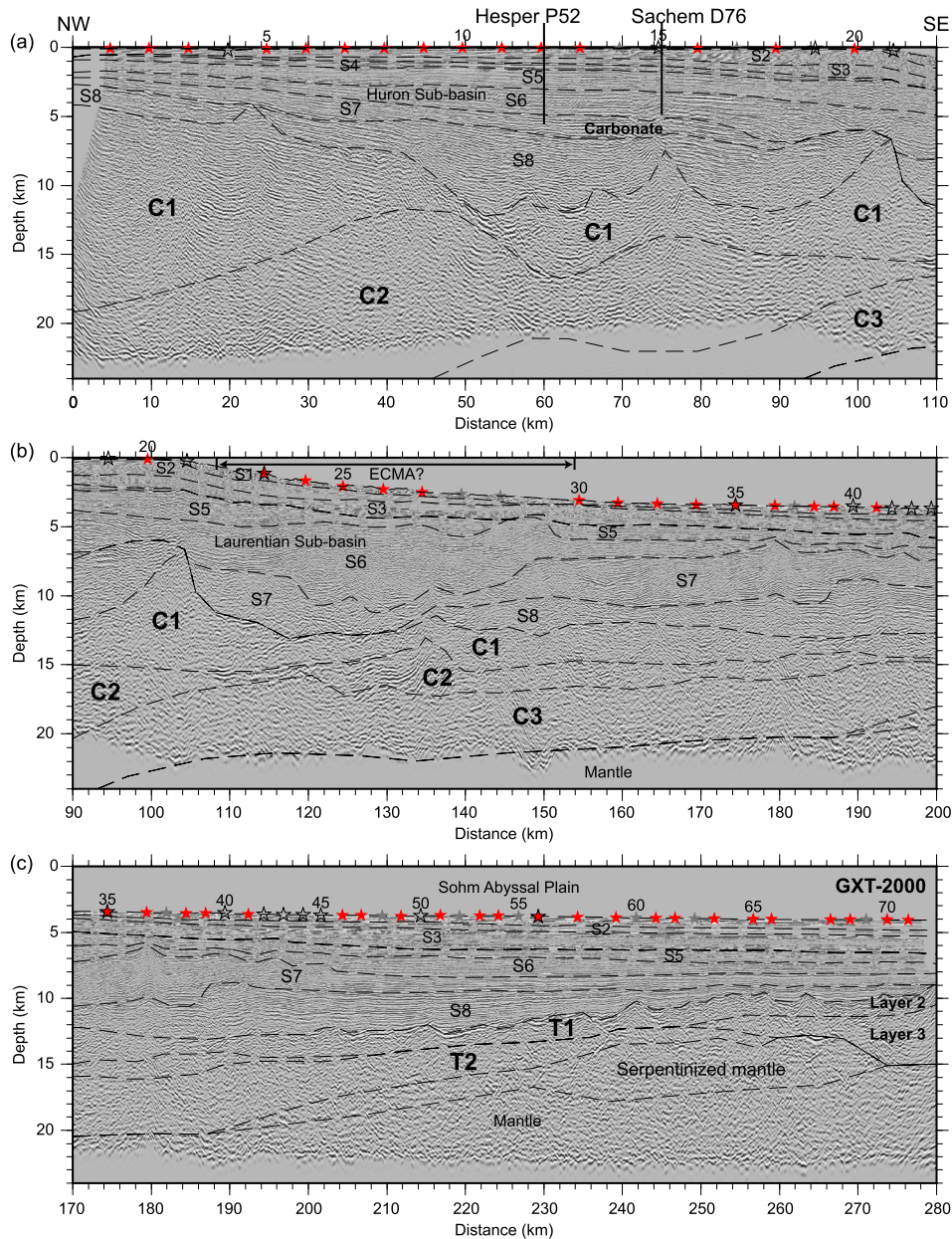
Figure A1. Same as Figure 14 with MCS profile GXT-2000 seismic amplitude plotted in grayscale and the OETR-2009 final velocity model boundaries in black dashed lines. MCS = multichannel seismic.

scale continental orphan blocks toward the formation of embryonic oceanic crust. The lower crust is best interpreted as moderately (50–70%) serpentinized mantle.

5. A well-constrained low velocity (7.1–8.0 km/s) mantle layer interpreted as partially (<50%) serpentinized mantle is modeled beneath the transitional crust. Being <2-km thick in the landward subzone, it thickens steeply to >4 km in the seaward subzone. We do not, however, observe exhumed mantle.

6. Systematic accretion of oceanic crust is proposed farther seaward beneath the Sohm Abyssal Plain ~170 km from the shelf break, as velocities typical of oceanic Layer 2 (5.0–5.9 km/s) and Layer 3 (6.2–7.4 km/s) are modeled. Its relatively small total thickness (3.5–6 km) indicates low melt supply even during seafloor spreading.

7. A reconstruction of the Nova Scotia-Morocco conjugate system shows margin asymmetry in crustal structural smoothness and thickness, in width, and in seafloor and basement depths. However, considering the

similarity in the region around the boundary between the continental and transitional zones, we argue that the landward oceanic zone previously interpreted for the Moroccan margin (Biari et al., 2015) is equivalent to our transitional zone and that only a 16 km eastward ridge jump is required to explain the asymmetry. Additional asymmetries are also a result of a presence of postrift volcanism from the Canary Plume on the Moroccan side. Despite the asymmetries, we interpret rifting to have been amagmatic on both sides.

Appendix A: Supplementary Plot

Figure A1 shows the MCS profile GXT-2000 for comparison with the OETR-2009 model boundaries. Contrast between high- and low-amplitude reflections is better represented using gray scale than variable area traces due to the small size of plots.

References

Aghaei, O., Nedimović, M. R., Carton, H., Carbotte, S. M., Canales, J. P., & Mutter, J. C. (2014). Crustal thickness and Moho character of the fast-spreading East Pacific Rise from 9°42′N to 9°57′N from poststack-migrated 3-D MCS data. *Geochemistry, Geophysics, Geosystems*, *15*, 634–657. https://doi.org/10.1002/2013GC005069

Albertz, M., & Beaumont, C. (2010). An investigation of salt tectonic structural styles in the Scotian Basin, offshore Atlantic Canada: 2. Comparison of observations with geometrically complex numerical models. *Tectonics*, *29*, TC4018. https://doi.org/10.1029/2009TC002540

Barr, S. M., & Raeside, R. P. (1989). Tectono-stratigraphic terranes in Cape Breton Island, Nova Scotia: Implications for the configuration of the northern Appalachian orogen. *Geology*, *17*(9), 822. https://doi.org/10.1130/0091-7613(1989)017<0822:TSTICB>2.3.CO;2

Barss, M. S., Bujak, J. P., & Williams, G. L. (1979). Palynological zonation and correlation of sixty-seven wells, eastern Canada. Geol Surv Canada Paper 78–24, 118.

BASIN Database Team (2017). The BASIN Database. Retrieved from http://basin.gdr.nrcan.gc.ca/index_e.php

Bayrakci, G., Minshull, T. A., Sawyer, D. S., Reston, T. J., Klaeschen, D., Papenberg, C., et al. (2016). Fault-controlled hydration of the upper mantle during continental rifting. *Nature Geoscience*, *9*(5), 384–388. https://doi.org/10.1038/ngeo2671

Beaumont, C. (2010). PFA atlas annex 10: Report on continuation of OETR Nova Scotia margin project: Forward dynamical modeling of 1 Margin development during rifting and 2 Salt tectonics. In *ATLAS: Play fairway analysis offshore Nova Scotia* (Appendix 1A, pp. 22–44). Halifax, Nova Scotia: Department of Energy. Retrieved from https://energy.novascotia.ca/sites/default/files/files/Annex-10_Report%20Beaumont_Salt%20Tectonics.zip

Benabdellouahed, M., Klingelhoefer, F., Gutscher, M.-A., Rabineau, M., Biari, Y., Hafid, M., et al. (2017). Recent uplift of the Atlantic Atlas (offshore West Morocco): Tectonic arch and submarine terraces. *Tectonophysics*, *706-707*, 46–58. https://doi.org/10.1016/j.tecto.2017.03.024

Biari, Y., Klingelhoefer, F., Sahabi, M., Aslanian, D., Schnurle, P., Berglar, K., et al. (2015). Deep crustal structure of the North-West African margin from combined wide-angle and reflection seismic data (MIRROR seismic survey). *Tectonophysics*, *656*, 154–174. https://doi.org/10.1016/j.tecto.2015.06.019

Biari, Y., Klingelhoefer, F., Sahabi, M., Funck, T., Benabdellouahed, M., Schnabel, M., et al. (2017). Opening of the central Atlantic Ocean: Implications for geometric rifting and asymmetric initial seafloor spreading after continental breakup. *Tectonics*, *36*, 1129–1150. https://doi.org/10.1002/2017TC004596

Bird, D. E., Hall, S. A., Burke, K., Casey, J. F., & Sawyer, D. S. (2007). Early Central Atlantic Ocean seafloor spreading history. *Geosphere*, *3*(5), 282. https://doi.org/10.1130/GES00047.1

Brune, S., Heine, C., Clift, P. D., & Pérez-Gussinyé, M. (2017). Rifted margin architecture and crustal rheology: Reviewing Iberia-Newfoundland, Central South Atlantic, and South China Sea. *Marine and Petroleum Geology*, *79*, 257–281. https://doi.org/10.1016/j.marpetgeo.2016.10.018

Brune, S., Heine, C., Pérez-Gussinyé, M., & Sobolev, S. V. (2014). Rift migration explains continental margin asymmetry and crustal hyper-extension. *Nature Communications*, *5*, 4014. https://doi.org/10.1038/ncomms5014

Contrucci, I., Klingelhöfer, F., Perrot, J., Bartolome, R., Gutscher, M.-A., Sahabi, M., et al. (2004). The crustal structure of the NW Moroccan continental margin from wide-angle and reflection seismic data. *Geophysical Journal International*, *159*(1), 117–128. https://doi.org/10.1111/j.1365-246X.2004.02391.x

Davy, R. G., Minshull, T. A., Bayrakci, G., Bull, J. M., Klaeschen, D., Papenberg, C., et al. (2016). Continental hyperextension, mantle exhumation, and thin oceanic crust at the continent-ocean transition, West Iberia: New insights from wide-angle seismic: Continent-ocean transition at the deep galicia margin. *Journal of Geophysical Research: Solid Earth*, *121*, 3177–3199. https://doi.org/10.1002/2016JB012825

Dehler, S. A. (2012). Initial rifting and breakup between Nova Scotia and Morocco: Insight from new magnetic models. *Canadian Journal of Earth Sciences*, *49*(12), 1385–1394. https://doi.org/10.1139/e2012-073

Dick, H. J. B., Lin, J., & Schouten, H. (2003). An ultraslow-spreading class of ocean ridge. *Nature*, *426*(6965), 405–412. https://doi.org/10.1038/nature02128

Funck, T., Hopper, J. R., Larsen, H. C., Louden, K. E., Tucholke, B. E., & Holbrook, W. S. (2003). Crustal structure of the ocean-continent transition at Flemish Cap: Seismic refraction results. *Journal of Geophysical Research*, *108*(B11), 2531. https://doi.org/10.1029/2003JB002434

Funck, T., Jackson, H. R., Louden, K. E., Dehler, S. A., & Wu, Y. (2004). Crustal structure of the northern Nova Scotia rifted continental margin (eastern Canada). *Journal of Geophysical Research*, *109*, B09102. https://doi.org/10.1029/2004JB003008

General Bathymetric Chart of the Oceans (2008). General bathymetric chart of the oceans (GEBCO) one minute grid. Retrieved from https://www.bodc.ac.uk/data/hosted_data_systems/gebco_gridded_bathymetry_data/gebco_one_minute_grid/

Gradstein, F. M., Ogg, J. G., & Smith, A. G. (2004). *A geologic time scale 2004*. Cambridge, UK: Cambridge University Press.

Holbrook, W. S., & Kelemen, P. B. (1993). Large igneous province on the US Atlantic margin and implications for magmatism during continental breakup. *Nature*, *364*(6436), 433–436. https://doi.org/10.1038/364433a0

Holik, J. S., Rabinowitz, P. D., & Austin, J. A. (1991). Effects of Canary hotspot volcanism on structure of oceanic crust off Morocco. *Journal of Geophysical Research: Solid Earth*, *96*, 12,039–12,067. https://doi.org/10.1029/91JB00709

Huismans, R., & Beaumont, C. (2011). Depth-dependent extension, two-stage breakup and cratonic underplating at rifted margins. *Nature*, *473*(7345), 74–78. https://doi.org/10.1038/nature09988

Huismans, R. S., & Beaumont, C. (2003). Symmetric and asymmetric lithospheric extension: Relative effects of frictional-plastic and viscous strain softening. *Journal of Geophysical Research*, *108*(B10), 2496. https://doi.org/10.1029/2002JB002026

Jansa, L. F., & Wade, J. A. (1975). Geology of the continental margin off Nova Scotia and Newfoundland. In *Geological survey of Canada paper 74–30, offshore geology of eastern Canada* (Vol. 2, pp. 51–105). Ottawa, Canada: Energy, Mines and Resources.

Keen, C. E., & Cordsen, A. (1981). Crustal structure, seismic stratigraphy, and rift processes of the continental margin off eastern Canada: Ocean bottom seismic refraction results off Nova Scotia. *Canadian Journal of Earth Sciences*, *18*(10), 1523–1538. https://doi.org/10.1139/e81-142

Keen, C. E., MacLean, B. C., & Kay, W. A. (1991). A deep seismic reflection profile across the Nova Scotia continental margin, offshore eastern Canada. *Canadian Journal of Earth Sciences*, *28*(7), 1112–1120. https://doi.org/10.1139/e91-100

Keen, C. E., & Potter, D. P. (1995a). The transition from a volcanic to a nonvolcanic rifted margin off eastern Canada. *Tectonics*, *14*, 359–371. https://doi.org/10.1029/94TC03090

Keen, C. E., & Potter, D. P. (1995b). Formation and evolution of the Nova Scotian rifted margin: Evidence from deep seismic reflection data. *Tectonics*, *14*, 918–932. https://doi.org/10.1029/95TC00838

Klingelhoefer, F., Biari, Y., Sahabi, M., Aslanian, D., Schnabel, M., Matias, L., et al. (2016). Crustal structure variations along the NW-African continental margin: A comparison of new and existing models from wide-angle and reflection seismic data. *Tectonophysics*, *674*, 227–252. https://doi.org/10.1016/j.tecto.2016.02.024

Klitgord, K. D., & Schouten, H. (1986). Plate kinematics of the central Atlantic. In P. R. Vogt & B. E. Tucholke (Eds.), *The western north Atlantic region* (Vol. M, pp. 351–378). Boulder, CO: Geological Society of America.

Labails, C., Olivet, J.-L., Aslanian, D., & Roest, W. R. (2010). An alternative early opening scenario for the Central Atlantic Ocean. *Earth and Planetary Science Letters*, *297*(3–4), 355–368. https://doi.org/10.1016/j.epsl.2010.06.024

Lau, K. W. H., Louden, K. E., Funck, T., Tucholke, B. E., Holbrook, W. S., Hopper, J. R., & Christian Larsen, H. (2006). Crustal structure across the Grand Banks–Newfoundland Basin Continental Margin—I. Results from a seismic refraction profile. *Geophysical Journal International*, *167*(1), 127–156. https://doi.org/10.1111/j.1365-246X.2006.02988.x

Lau, K. W. H., Watremez, L., Louden, K. E., & Nedimović, M. R. (2015). Structure of thinned continental crust across the Orphan Basin from a dense wide-angle seismic profile and gravity data. *Geophysical Journal International*, *202*(3), 1969–1992. https://doi.org/10.1093/gji/ggv261

Louden, K., Wu, Y., & Tari, G. (2013). Systematic variations in basement morphology and rifting geometry along the Nova Scotia and Morocco conjugate margins. *Geological Society, London, Special Publications*, *369*(1), 267–287. https://doi.org/10.1144/SP369.9

Louden, K. E., & Chian, D. (1999). The deep structure of non–volcanic rifted continental margins. *Philosophical Transactions of the Royal Society of London, Series A: Mathematical, Physical and Engineering Sciences*, *357*(1753), 767. https://doi.org/10.1098/rsta.1999.0352

Louden, K. E., Osler, J. C., Srivastava, S. P., & Keen, C. E. (1996). Formation of oceanic crust at slow spreading rates: New constraints from an extinct spreading center in the Labrador Sea. *Geology*, *24*(9), 771. https://doi.org/10.1130/0091-7613(1996)024<0771:FOOCAS>2.3.CO;2

Louden, K. E., Wallace, D. O., & Courtney, R. C. (1987). Heat flow and depth versus age for the Mesozoic northwest Atlantic Ocean: Results from the Sohm abyssal plain and implications for the Bermuda rise. *Earth and Planetary Science Letters*, *83*(1–4), 109–122. https://doi.org/10.1016/0012-821X(87)90055-0

Luheshi, M., Roberts, D. G., Nunn, K., Makris, J., Colletta, B., Wilson, H., et al. (2012). The impact of conjugate margins analysis on play fairway evaluation—An analysis of the hydrocarbon potential of Nova Scotia. *First Break*, *30*(1814). https://doi.org/10.3997/1365-2397.2011037

MacLean, B. C., & Wade, J. A. (1993). *East coast basin atlas series: Seismic markers and stratigraphic picks in Scotian Basin wells* (p. 276). Ottawa, Canada: Atlantic Geoscience Centre, Geological Survey of Canada. Retrieved from http://ftp.maps.canada.ca/pub/nrcan_rncan/publications/ess_sst/221/221116/ecbas_1993.pdf

Maillard, A., Malod, J., Thiébot, E., Klingelhoefer, F., & Réhault, J.-P. (2006). Imaging a lithospheric detachment at the continent–ocean crustal transition off Morocco. *Earth and Planetary Science Letters*, *241*(3–4), 686–698. https://doi.org/10.1016/j.epsl.2005.11.013

Maystrenko, Y., & Scheck-Wenderoth, M. (2009). Density contrasts in the upper mantle and lower crust across the continent-ocean transition: Constraints from 3-D gravity modelling at the Norwegian margin. *Geophysical Journal International*, *179*(1), 536–548. https://doi.org/10.1111/j.1365-246X.2009.04273.x

Müller, R. D., Sdrolias, M., Gaina, C., & Roest, W. R. (2008). Age, spreading rates, and spreading asymmetry of the world's ocean crust. *Geochemistry, Geophysics, Geosystems*, *9*, Q04006. https://doi.org/10.1029/2007GC001743

Newman, K. R., Nedimović, M. R., Canales, J. P., & Carbotte, S. M. (2011). Evolution of seismic layer 2B across the Juan de Fuca Ridge from hydrophone streamer 2-D traveltime tomography: Evolution of seismic layer 2B. *Geochemistry, Geophysics, Geosystems*, *12*, Q05009. https://doi.org/10.1029/2010GC003462

Pérez-Gussinyé, M., Ranero, C. R., Reston, T. J., & Sawyer, D. (2003). Mechanisms of extension at nonvolcanic margins: Evidence from the Galicia interior basin, west of Iberia. *Journal of Geophysical Research*, *108*(B5), 2245. https://doi.org/10.1029/2001JB000901

Pérez-Gussinyé, M., & Reston, T. J. (2001). Rheological evolution during extension at nonvolcanic rifted margins: Onset of serpentinization and development of detachments leading to continental breakup. *Journal of Geophysical Research*, *106*, 3961–3975. https://doi.org/10.1029/2000JB900325

Play Fairway Analysis Atlas (2011). Play fairway analysis atlas. Retrieved from https://energy.novascotia.ca/oil-and-gas/offshore/play-fairway-analysis/analysis

Prosser, S. (1993). Rift-related linked depositional systems and their seismic expression. *Geological Society, London, Special Publications*, *71*(1), 35–66. https://doi.org/10.1144/GSL.SP.1993.071.01.03

Ranero, C. R., & Pérez-Gussinyé, M. (2010). Sequential faulting explains the asymmetry and extension discrepancy of conjugate margins. *Nature*, *468*(7321), 294–299. https://doi.org/10.1038/nature09520

Reston, T. J. (2009). The structure, evolution and symmetry of the magma-poor rifted margins of the North and Central Atlantic: A synthesis. *Tectonophysics*, *468*(1–4), 6–27. https://doi.org/10.1016/j.tecto.2008.09.002

Ros, E., Pérez-Gussinyé, M., Araújo, M., Thoaldo Romeiro, M., Andrés-Martínez, M., & Morgan, J. P. (2017). Lower crustal strength controls on melting and serpentinization at magma-poor margins: Potential implications for the South Atlantic. *Geochemistry, Geophysics, Geosystems*, *18*, 4538–4557. https://doi.org/10.1002/2017GC007212

Sahabi, M., Aslanian, D., & Olivet, J.-L. (2004). Un nouveau point de départ pour l'histoire de l'Atlantique central. *Comptes Rendus Geoscience*, *336*(12), 1041–1052. https://doi.org/10.1016/j.crte.2004.03.017

Sandwell, D. T., Müller, R. D., Smith, W. H. F., Garcia, E., & Francis, R. (2014). New global marine gravity model from CryoSat-2 and Jason-1 reveals buried tectonic structure. *Science*, *346*(6205), 65–67. https://doi.org/10.1126/science.1258213

Schettino, A., & Turco, E. (2009). Breakup of Pangaea and plate kinematics of the central Atlantic and Atlas regions. *Geophysical Journal International*, *178*(2), 1078–1097. https://doi.org/10.1111/j.1365-246X.2009.04186.x

Seton, M., Müller, R. D., Zahirovic, S., Gaina, C., Torsvik, T., Shephard, G., et al. (2012). Global continental and ocean basin reconstructions since 200Ma. *Earth-Science Reviews*, *113*(3-4), 212–270. https://doi.org/10.1016/j.earscirev.2012.03.002

Shimeld, J. (2004). A Comparison of Salt Tectonic Subprovinces beneath the Scotian Slope and Laurentian Fan. In P. Post, et al. (Eds.), *GCSSEPM 24th annual Bob F. Perkins research conference, salt sediment interactions and hydrocarbon prospectivity: Concepts, applications, and case studies for the 21st century*, *Gulf Coast Section* (Vol. 24, pp. 291–306). Houston, TX: SEPM Foundation. https://doi.org/10.5724/gcs.04.24.0502

Sibuet, J.-C., Rouzo, S., & Srivastava, S. (2012). Plate tectonic reconstructions and paleogeographic maps of the central and North Atlantic oceans. *Canadian Journal of Earth Sciences*, *49*(12), 1395–1415. https://doi.org/10.1139/e2012-071

Talwani, M., & Abreu, V. (2000). In W. Mohriak & M. Taiwani (Eds.), *Inferences regarding initiation of oceanic crust formation from the U.S. East Coast margin and conjugate South Atlantic margins*, *Geophysical Monograph Series* (Vol. 115, pp. 211–233). Washington, DC: American Geophysical Union. https://doi.org/10.1029/GM115p0211

Talwani, M., Worzel, J. L., & Landisman, M. (1959). Rapid gravity computations for two-dimensional bodies with application to the Mendocino submarine fracture zone. *Journal of Geophysical Research*, *64*, 49–59. https://doi.org/10.1029/JZ064i001p00049

Tari, G., & Molnar, J. (2005). Correlation of Syn-rift structures between Morocco and Nova Scotia, Canada. GCSSEPM Transactions (pp. 132–150). https://doi.org/10.5724/gcs.05.25.0132

Wade, J. A., & Maclean, B. C. (1990). Aspects of the Geology of the Scotian Basin from Recent Seismic and Well Data (No. 2). https://doi.org/10.4095/132704

Wade, J. A., Williams, G. L., & MacLean, B. C. (1995). Mesozoic and Cenozoic stratigraphy, eastern Scotian shelf: New interpretations. *Canadian Journal of Earth Sciences*, *32*(9), 1462–1473. https://doi.org/10.1139/e95-118

Watanabe, T., Kasami, H., & Ohshima, S. (2007). Compressional and shear wave velocities of serpentinized peridotites up to 200 MPa. *Earth, Planets and Space*, *59*(4), 233–244. https://doi.org/10.1186/BF03353100

Watremez, L., Lau, K. W. H., Nedimović, M. R., & Louden, K. E. (2015). Traveltime tomography of a dense wide-angle profile across Orphan Basin. *Geophysics*, *80*(3), B69–B82. https://doi.org/10.1190/geo2014-0377.1

Welsink, H. J., Dwyer, J. D., & Knight, R. J. (1989). Tectono-stratigraphy of the passive margin off Nova Scotia. In A. J. Tankard & H. R. Balkwill (Eds.), *Extensional tectonics and stratigraphy of the North Atlantic margin*, *Memoir* (Vol. 46, pp. 215–231). Tulsa, OK: American Association of Petroleum Geologists.

Wenker, S., & Beaumont, C. (2016). Effects of lateral strength contrasts and inherited heterogeneities on necking and rifting of continents. *Tectonophysics*. https://doi.org/10.1016/j.tecto.2016.10.011

White, R. S., McKenzie, D., & O'Nions, R. K. (1992). Oceanic crustal thickness from seismic measurements and rare earth element inversions. *Journal of Geophysical Research*, *97*, 19,683–19,715. https://doi.org/10.1029/92JB01749

Williams, H. (1979). Appalachian orogen in Canada. *Canadian Journal of Earth Sciences*, *16*(3), 792–807. https://doi.org/10.1139/e79-070

Won, I. J., & Bevis, M. (1987). Computing the gravitational and magnetic anomalies due to a polygon; algorithms and Fortran subroutines. *Geophysics*, *52*(2), 232–238. https://doi.org/10.1190/1.1442298

Wu, Y., Louden, K. E., Funck, T., Jackson, H. R., & Dehler, S. A. (2006). Crustal structure of the central Nova Scotia margin off Eastern Canada. *Geophysical Journal International*, *166*(2), 878–906. https://doi.org/10.1111/j.1365-246X.2006.02991.x

Zelt, C. A., & Smith, R. B. (1992). Seismic traveltime inversion for 2-D crustal velocity structure. *Geophysical Journal International*, *108*(1), 16–34. https://doi.org/10.1111/j.1365-246X.1992.tb00836.x